Applying stochastic spike train theory for high-accuracy human MEG/EEG

Trusbak Haumann, Niels

2020-07-01

Trusbak Haumann , N , Hansen , B , Huotilainen , M , Vuust , P & Brattico , E 2020 , ' Applying stochastic spike train theory for high-accuracy human MEG/EEG ' , Journal of Neuroscience Methods , vol. 340 , 108743 . https://doi.org/10.1016/j.jneumeth.2020.108743

http://hdl.handle.net/10138/315793
https://doi.org/10.1016/j.jneumeth.2020.108743

Journal of Neuroscience Methods 340 (2020) 108743

Contents lists available at ScienceDirect

Journal of Neuroscience Methods

journal homepage: www.elsevier.com/locate/jneumeth

Applying stochastic spike train theory for high-accuracy human MEG/EEG

Niels Trusbak Haumann[a,*], Brian Hansen[b], Minna Huotilainen[c], Peter Vuust[a], Elvira Brattico[a,d,e]

[a] Center for Music in the Brain, Department of Clinical Medicine, Aarhus University and Royal Academy of Music, Aarhus/Aalborg, Nørrebrogade 44, 8000 Aarhus C, Denmark
[b] Center of Functionally Integrative Neuroscience, Department of Clinical Medicine, Nørrebrogade 44, 8000 Aarhus C, Denmark
[c] Cognitive Brain Research Unit and CICERO Learning Network, University of Helsinki, P.O. Box 9, Helsinki FIN-00014, Finland
[d] BioMag Laboratory, HUS Medical Imaging Center, University of Helsinki and Helsinki University Hospital, 00100 Helsinki, Finland
[e] Department of Education, Psychology, Communication, University of Bari Aldo Moro, Italy

ARTICLE INFO

Keywords:
Neuronal spike trains
EEG
MEG
Component analysis
Single-subject analysis

ABSTRACT

Background: The accuracy of electroencephalography (EEG) and magnetoencephalography (MEG) in measuring neural evoked responses (ERs) is challenged by overlapping neural sources. This lack of accuracy is a severe limitation to the application of ERs to clinical diagnostics.
New method: We here introduce a theory of stochastic neuronal spike timing probability densities for describing the large-scale spiking activity in neural assemblies, and a spike density component analysis (SCA) method for isolating specific neural sources. The method is tested in three empirical studies with 564 cases of ERs to auditory stimuli from 94 humans, each measured with 60 EEG electrodes and 306 MEG sensors, and a simulation study with 12,300 ERs.
Results: The first study showed that neural sources (but not non-encephalic artifacts) in individual averaged MEG/EEG waveforms are modelled accurately with temporal Gaussian probability density functions (median 99.7 %–99.9 % variance explained). The following studies confirmed that SCA can isolate an ER, namely the mismatch negativity (MMN), and that SCA reveals inter-individual variation in MMN amplitude. Finally, SCA reduced errors by suppressing interfering sources in simulated cases.
Comparison with existing methods: We found that gamma and sine functions fail to adequately describe individual MEG/EEG waveforms. Also, we observed that principal component analysis (PCA) and independent component analysis (ICA) does not consistently suppress interference from overlapping brain activity in neither empirical nor simulated cases.
Conclusions: These findings suggest that the overlapping neural sources in single-subject or patient data can be more accurately separated by applying SCA in comparison to PCA and ICA.

1. Introduction

1.1. Present limitations in MEG/EEG

Electroencephalography (EEG) and magnetoencephalography (MEG) methods are among the most applied in human neuroscience (Duncan et al., 2009; Tong and Thakor, 2009). The latest MEG/EEG protocols test advanced cognitive processes and detailed perceptual discrimination abilities for tasks and stimuli of increasing complexity (Puce and Hämäläinen, 2017). However, with increasingly complex protocols the neural sources often need to be obtained from fewer measurement samples and show smaller amplitudes compared to other interfering brain activity (Cong et al., 2010). A general problem is that the evoked response of interest becomes difficult to isolate, and the analysis of functional changes in a specific response is often inaccurate and unreliable at the single-subject level (Litvak et al., 2013; Nikulin et al., 2011; Scharf and Nestler, 2018). This leads to low replication rates (Luck and Gaspelin, 2017) and limits the translation of basic MEG/EEG research findings into clinical applications with the individual patient (Armanfard et al., 2018; Bishop and Hardiman, 2010).

1.2. Isolating the component of interest from a mixture of components

The measured evoked response MEG/EEG waveforms contain a summation of overlapping latent components which must be separated analytically (Luck, 2014). A common solution for isolating a specific component of interest is the use of a functional localizer (Luck and Gaspelin, 2017), or analysis window. The time range and the channel

* Corresponding author.
E-mail addresses: niels.haumann@clin.au.dk (N.T. Haumann), minna.huotilainen@helsinki.fi (M. Huotilainen).

https://doi.org/10.1016/j.jneumeth.2020.108743
Received 24 April 2019; Received in revised form 14 April 2020; Accepted 14 April 2020
Available online 25 April 2020

selection for the analysis window are conventionally defined based on the maximum amplitude response in the grand average signal across a group of subjects. A weakness of this method is, however, that other neural sources can remain interfering with the evoked response of interest within the analysis window. Also, a narrow analysis window might result in analytical bias, caused by possible inter-subject variation in the latency and location of the response of interest that may occur outside the analysis window (Luck and Gaspelin, 2017).

1.3. Source location modelling

Another solution is to separate the overlapping responses by modelling the locations and orientations of the neural sources and their projections through the brain and skull onto the extracranial MEG sensors or EEG electrodes (Wendel et al., 2009). However, when more sources are simultaneously present and the signal-to-noise and interference ratio (SNIR) (including the interference from spatially and temporally overlapping neural activity originating from different brain regions) is low, source location errors of up to centimeters and distorted source waveforms are commonly observed (Kiebel et al., 2008; Schwartz et al., 1999; Sharon et al., 2007; Vanrumste et al., 2001; Whittingstall et al., 2003; Zumer et al., 2008). Recently, it has been considered that part of the source location modelling errors may originate from the simultaneous estimation of the source amplitudes, locations, orientations, and projections within a single model (Wendel et al., 2009). Instead, it has been proposed to first separate the mixed sources with blind source separation, prior to modelling the locations and orientations of the sources (Reynolds and Richards, 2009; Richards, 2004; Tsai et al., 2006; Vigario et al., 2000; Zhukov et al., 2000).

1.4. Blind source separation

With blind source separation applied for MEG/EEG, each component is commonly assumed to have a consistent spatial distribution, or topography (Jung et al., 1998). The component topography is represented by a linear weighting vector that defines the magnitude and polarity of the projection of the component waveform onto each MEG/EEG channel, which is often estimated with principal component analysis (PCA) or independent component analysis (ICA) (Choi et al., 2005). However, a general weakness of the blind source separation methods is that they cannot separate temporally overlapping sources with similar spatial topographies, and they do not distinguish between sources based on their polarity (Groppe et al., 2008). The spatial topography and the polarity are crucial characteristics for identifying sources originating from the brain, and sources with similar spatial topographies are common in MEG/EEG paradigms (Picton et al., 1974). Therefore, we here suggest applying a novel spike density component analysis (SCA) method, which in addition to the spatial topography also models the polarity and temporal shape. Recent work has applied temporal PCA to estimate consistent temporal components, in addition to spatial blind source separation for estimating consistent spatial components (Dien, 2010; Dien et al., 2005, 2007; Kayser and Tenke, 2003). The present work focuses on modelling physiologically constrained temporal shapes reflecting the large-scale activity constituted by individual behavior of the neurons in brain networks.

1.5. Large-scale stochastic neuronal spike trains

The electrical potentials measured with EEG and the magnetic fields measured with MEG originate from large-scale spiking activity of neurons and the resulting postsynaptic potentials in neural networks (Buzsaki et al., 2012; Deco et al., 2008; Hämäläinen et al., 1993). Each spike of the single neuron involves an action potential in the axon appearing typically for durations on the range of 1 ms and a synaptic current flow with a duration in the range of 10 ms, which typically results in a local voltage change of 25 mV and a magnetic field of 20 fAm across 0.1–0.2 mm (Hämäläinen et al., 1993). The spiking activity observed in intracranial recordings of the electrophysiological responses to auditory, visual or tactile stimuli of single cortical or subcortical neurons is commonly analyzed with a peristimulus time histogram (PSTH) (Brown et al., 2004; deCharms and Merzenich, 1996; Dorrscheidt, 1981; Filali et al., 2004; Gerstein and Mandelbrot, 1964; Mukamel et al., 2010; Rodieck, 1962; Shimazaki and Shinomoto, 2007). The PSTH shows the number of spikes counted in time bins, i.e., the momentary firing rate in spikes per second, in a time window locked to the beginning of a stimulus. The spikes in each time bin are counted across a series of trials of repeated stimulation. Whereas the spike timing of the single neuron after each single stimulation appears to be random, the accumulated spike timing across a series of trials reveals systematic distributions of the spikes across time, which can be described with stochastic spike density functions (Barbieri et al., 2001; Brown et al., 2004; Gerstein and Mandelbrot, 1964; Maimon and Assad, 2009; Rodieck, 1962; Stein et al., 2005; Teramae and Fukai, 2014).

The spike densities, observed as variance in the spike timing of the single neuron, have been considered to originate from a large-scale principle of stochastic resonance in neural assemblies, which depends on the organization of the synaptic pathways (Stein et al., 2005; Teramae and Fukai, 2014). While the spike timing variability in single neurons is commonly described with stochastic functions (Aljadeff et al., 2016; Barbieri et al., 2001; Gerstein and Mandelbrot, 1964; Maimon and Assad, 2009; Shin, 2002; Stein et al., 2005; Teramae and Fukai, 2014), it has not yet been investigated how the stochastic variance in spike timing might be reflected in EEG and MEG. PSTHs for peripheral neurons show regular clock-like spike patterns with low variability in the spike timing, such as in neurons in the brain stem, while in pyramidal cortical neurons, in particular in association areas, there is higher variability in spike timing, as observed with intracranial single neuron recordings (Maimon and Assad, 2009). Interestingly, non-invasive scalp EEG recordings of evoked responses from the human brain stem reveal similar narrow time distributions of each brainstem response component (I, II, III, IV, V, VI), while the cortical evoked responses (N1, P2, N2) observed from cortical regions exhibit similar broader temporal distributions (Picton et al., 1974). Based on these considerations, we suggest that, in addition to single-neuron spike timing behavior, also large-scale neuronal activity in MEG/EEG waveforms may be systematically described with stochastic spike density functions (Fig. 1). We here apply the term ‘spike density’ heuristically by acknowledging that the single neuronal spikes are not directly measured in the large-scale MEG/EEG waveforms. The spikes produced by the presynaptic neurons initiate synaptic currents, which cause the post-synaptic potentials, and the propagation of the post-synaptic potentials within and across the biological tissues results in the electromagnetic changes that are measured with MEG/EEG (Buzsaki et al., 2012; Deco et al., 2008; Hämäläinen et al., 1993).

The main generators of the post-synaptic potentials observed in MEG/EEG waveforms are cortical pyramidal neurons from layers IV–V (Friston, 2005; Hämäläinen et al., 1993). At the micrometer scale of the single neuron, the spike timing of the cortical pyramidal cell has often been described as a Poisson process (Aljadeff et al., 2016; Barbieri et al., 2001; Gerstein and Mandelbrot, 1964; Kass et al., 2003; Maimon and Assad, 2009; Stein et al., 2005; Teramae and Fukai, 2014; Waldert et al., 2013). At the centimeter scale of electrocorticography (ECoG), EEG and MEG a large number of neurons are involved in generating the post-synaptic potentials (Hämäläinen et al., 1993) initiated by the Poisson-shaped spike densities, and Poisson processes with large numbers of events can be approximated by Gaussian probability density functions (Tseng, 1949). Also, a recent MEG/EEG simulation study (Beauducel, 2018) shows that temporal Gaussian functions can model the true morphology of temporally overlapping evoked response components more accurately in comparison to PCA and ICA. The study by Beauducel (2018) introducing the temporal Gaussian functions was based on simulated MEG/EEG waveforms, which were first

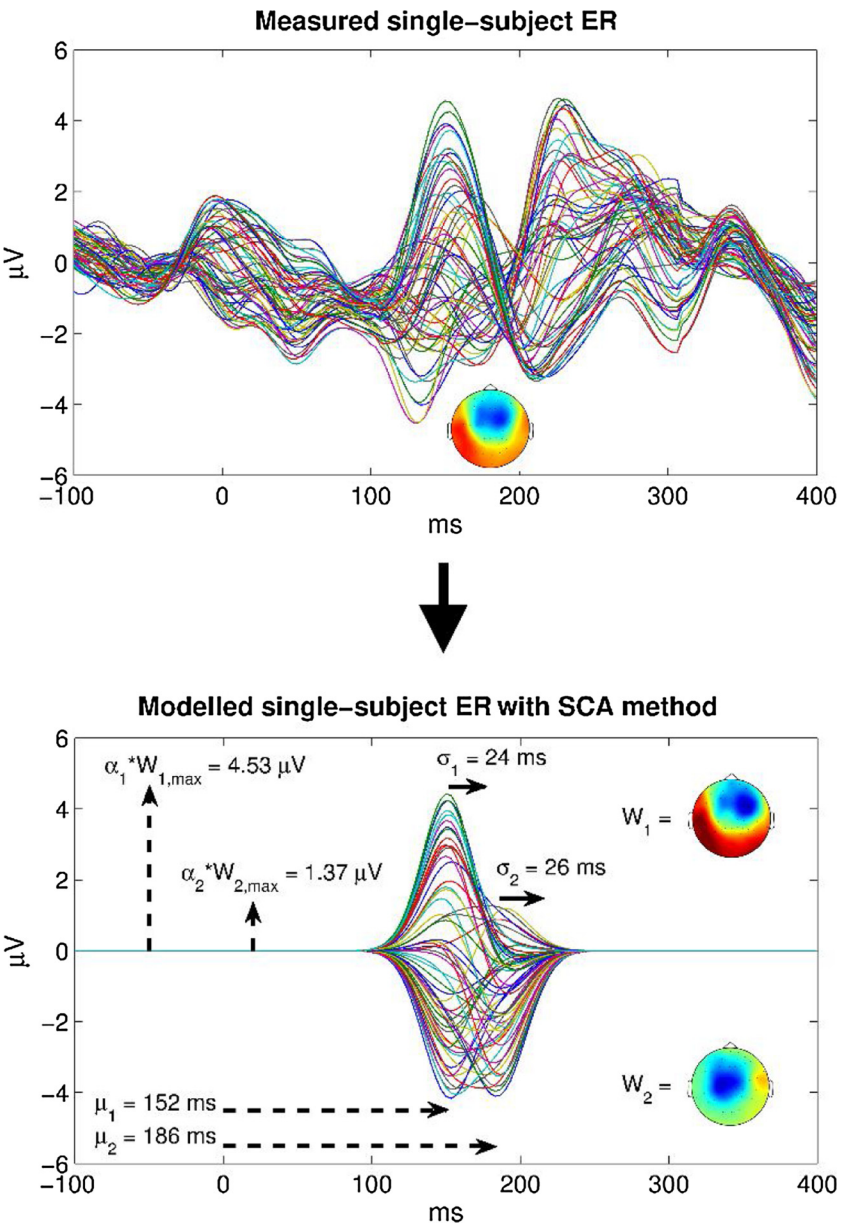

Fig. 1. Modelling single-subject EEG waveforms with stochastic spike density functions. The top panel shows an example of a butterfly plot and scalp topography for a single-subject average evoked response (ER) measured with EEG (here the mismatch negativity or MMN response). In the bottom, the parameters for the same data modelled with temporal Gaussian density functions are illustrated. For two optimally fitted Gaussian functions the parameters μ_1 and μ_2 denote the expected latencies and the σ_1 and σ_2 the standard deviations in the time domain; the parameters α_1 and α_2 indicate the MMN component amplitudes. The estimated projection's weights on the EEG electrodes are denoted W_1 and W_2; right to the butterfly plot the scalp topographies for W_1 and W_2 are shown (cold colors indicate negative values and warm colors positive values). (For interpretation of the references to colour in this figure legend, the reader is referred to the web version of this article.)

decomposed with temporal PCA, and the Gaussian functions were fitted to the temporal PCA components and optimized with Procrustes rotation. We here suggest that MEG/EEG waveforms measured from human subjects can be modelled directly by temporal Gaussian functions (see Methods section, Formula 1).

1.6. Research questions and hypotheses

In Study 1 we investigated whether single-subject average evoked responses (ERs) measured with EEG and MEG can be modelled by stochastic functions. The modelling performance of Gaussian functions was measured in percent explained variance and compared to the modelling performance of gamma and sine functions. Also, we investigated whether spike density component analysis (SCA) functions can specifically model the signals originating from the brain or other signals such as eye blink artifacts. This was tested by comparing the modelling performance and the residual signal peak amplitudes for SCA functions either with preprocessing or without preprocessing, in the last case including artifactual signals not originating from the brain.

In our second study we tested whether the SCA based on the Gaussian functions can be applied to accurately isolate a specific evoked brain response of interest, such as the mismatch negativity (MMN). Moreover, we investigated whether SCA isolates the MMN more accurately than principal component analysis (PCA) and independent component analysis (ICA). First, the root-mean-squared error (RMSE) of the remaining interfering signals in the baseline time points surrounding the MMN response was applied as a measure of the accuracy in suppressing interfering signals (the lower RMSE the higher accuracy). Also, the group-level ERs have a higher signal-to-interference and noise ratio (SNIR), since they are based on averages across more trials compared to the single-subject average waveforms, which contain more random interference and noise. This means that the group-level average of the individual ERs more closely reflects the true topography and waveform morphology of the ERs of interest compared to the individual ERs (Dien et al., 2007; Luck, 2014). Therefore, to test the ability of the MMN extraction methods to suppress the interference and noise in the single-subject ERs we correlated the extracted single-subject MMN with the group-level one with respect to spatial topography and temporal morphology (higher correlations indicate higher accuracy). Moreover, the number of estimated MMN-related

Table 1
Relationships between spike densities and MEG/EEG waveforms.

Waveform analysis	Spike density component analysis	Calculation from parameters of fitted Gaussian function
TIME DOMAIN		
Amplitude	*Maximum spike rate*	$\alpha\ (t)$
Latency	*Expected latency*	$\mu\ (t)$
–	*Spike timing uncertainty*	$\sigma\ (t)$
FREQUENCY DOMAIN		
Power	*Maximum spike rate of neural network loop*	$\alpha\ (f)$
Frequency	*Expected frequency of neural network loop*	$\mu\ (f)$
–	*Frequency bandwidth of neural network loop*	$\sigma\ (f) = 1/\sigma\ (t)$
Phase	*Expected time slot of neural network loop*	$\mu\ (p)$
–	*Time slot uncertainty of neural network loop*	$\sigma\ (p)$

components was investigated (fewer estimated components indicate higher accuracy).

Furthermore, in our third study we tested whether previous findings of individual differences in MMN amplitude related to depressive traits analyzed using conventional functional localizers (Bonetti et al., 2017) could be replicated with the SCA method.

Finally, in a fourth study we simulate EEG data to test how much MMN responses extracted with the SCA, ICA, and PCA methods diverge from known simulated MMN responses.

2. Materials and methods for study 1

2.1. Repository dataset

A pre-existing dataset was used consisting of 564 average ER waveforms recorded from 94 human subjects each exposed to six different experimental conditions under the "musical multi-feature no-standard" (muMUFEns) stimulus paradigm and recorded with 366 channel simultaneous EEG (60 electrodes) and MEG (102 axial MEG magnetometers, and 204 MEG planar gradiometers) at the Biomag Laboratory of the Helsinki University Central Hospital (for further details, see, e.g. Bonetti et al. (2017)). The MEG sensor positions were aligned according to the Elekta Neuromag Vectorview™ System (Elekta Neuromag®, Elekta Oy, Helsinki, Finland). A 64-channel EEG electrode cap following the modified 10–20 system was applied, and the ground electrode was placed on the right cheek and the reference electrode on the nose tip. All MEG/EEG data was recorded at a sampling rate of 1000 Hz. Informed consent was obtained from all participants. The dataset was a part of the data repository obtained under the research protocol named "Tunteet", approved by the Coordinating Ethics Committee of the Hospital District of Helsinki and Uusimaa (approval number: 315/13/03/00/11, obtained on March the 11th, 2012). Data are fully anonymized and here we only used processed data that have already been published. Specifically, findings related to studies 1–2 were previously published in studies on noise sensitivity (Kliuchko et al., 2016) and comparison of artifact correction methods (Haumann et al., 2016), and for study 3 in papers on the relationship between MMN amplitude and depressive traits (Bonetti et al., 2017) and working memory skills (Bonetti et al., 2018). The datasheets applied for statistical analyses in our studies are attached as supplementary materials.

2.2. Data preprocessing

MEG data was preprocessed with Elekta Neuromag™ MaxFilter 2.2 Temporal Signal Space Separation (tSSS) (Taulu and Hari, 2009) (with automatic detection and correction of bad MEG channels; default inside expansion order of 8; outside expansion order of 3; automatic optimization of both inside and outside bases; subspace correlation limit of 0.980; raw data buffer length of 10 s). Afterwards MEG and EEG data was further preprocessed with the FieldTrip toolbox for Matlab (version r9093, Donders Institute for Brain, Cognition and Behaviour/Max Planck Institute, Nijmegen, the Netherlands) (Oostenveld et al., 2011) and Matlab R2013b (MathWorks, Natick, Massachusetts). EEG and MEG waveforms were downsampled to 300 Hz, highpass filtered at 1 Hz, and lowpass filtered at 30 Hz. EEG channels were inspected and bad channels corrected with interpolation of the neighboring channels. Eye blink and ECG artifacts were inspected and corrected with ICA (Makeig et al., 1996). Trials were extracted for six experimental conditions consisting of (1) intensity, (2) location, (3) pitch, (4) rhythm, (5) slide, (6) timbre deviants and a standard condition. Any trials with amplitudes exceeding 100 μV, 2000 fT, or 400 fT/cm were rejected to reduce influence of potentially remaining artifacts. Averages across trials were obtained and average ER waveforms for the standard condition was subtracted from the deviant conditions to obtain the evoked MMN waveforms (for further details, see Bonetti et al. (2017)). A duplicate of the same average evoked MMN waveforms with presence of external artifactual signals was created by excluding the preprocessing procedures, before the trials and average MMN waveforms were extracted from the same dataset.

2.3. Spike density component analysis

Assuming that MEG/EEG waveforms in the time domain can be modelled with Gaussian functions (Eq. (1)), the α parameter describes the maximum spike rate, which is equivalent to the amplitude of a component in the MEG/EEG waveform (Table 1). The μ parameter denotes the expected latency, corresponding to the latency of a component in terms of conventional MEG/EEG waveform analysis, while the σ parameter defines the spike timing uncertainty or width of a component in the MEG/EEG waveform (Table 1).

$$\text{Gaussian function: } f(t\alpha, \mu, \sigma) = \alpha \frac{1}{\sigma\sqrt{2\pi}} e^{\frac{-(t-\mu)^2}{2\sigma^2}} \quad (1)$$

The Gaussian function applied in the time domain analysis will result in another Gaussian function applied in the frequency domain analysis (Bracewell and Bracewell, 1986). In the frequency domain, the α parameter describes the maximum spike rate of a neural network loop, equivalent to the observed power of the oscillation (Table 1). The μ parameter in the frequency domain defines the expected frequency of the neural network loop, and the μ parameter in the phase domain defines the expected time slot of the neural network loop (Table 1). The uncertainties in frequency and phase are represented by the σ parameters for frequency and phase (Table 1).

Another function often considered in spike density analysis is the gamma function (Eq. (2)) (Barbieri et al., 2001; Gerstein and Mandelbrot, 1964; Maimon and Assad, 2009). Here the shape parameter, k, defines the regularity of the spike timing, where higher value of k denotes more regular spike timing, which approaches a Gaussian distribution, while lower value of k denotes more random and skewed spike timing, differing from a Gaussian distribution (Maimon and Assad, 2009). For example, in the rhesus monkey neurons in the higher-level visual association area have been found to show more regular

spike timing, $k \approx 8$, compared to the more random and skewed spike timing of neurons in the lower level visual areas, $k < 5$ (Maimon and Assad, 2009).

$$\text{Gamma function: } f(t\alpha, k, \theta) = \alpha \frac{1}{\Gamma(k)\theta^k} t^{k-1} e^{\frac{-t}{\theta}} \quad (2)$$

Moreover, we suggest investigating the sine function (Eq. (3)), which is the foundation for the Fourier series and Morlet wavelets applied in analysis of narrowband oscillations in MEG/EEG waveforms: the theta, alpha, mu, beta, and gamma waves (Pfurtscheller and da Silva, 1999). Here it should be noted that the sine function reflects regular changes in the spike rate related to neural network loops involving polarity reversals (not to be confused with the frequency of the spike rate).

$$\text{Sine function: } f(t\alpha, \omega, \varphi) = \alpha \sin(\omega t + \varphi) \quad (3)$$

Spike density component analysis (SCA) in the time domain is performed on each average ER waveform by following an automatized iterative procedure (see Supplementary Materials Figure A.1) (example outputs are created with an open source FieldTrip-compatible Matlab function freely available at https://github.com/nielsthaumann/sca for decomposing any MEG/EEG/ECoG/iEEG data into SCA components). With SCA it is assumed that:

1 Components exist at signal-to-noise and interference ratios (SNIR) > 1. (SNIR here refers to background noise and artifacts, not overlapping components from the brain).
2 Components differ in time, width across time or topography

The SCA decomposition procedure is similar to PCA and Gaussian ER Procrustes analysis (Beauducel, 2018); though, since SCA and Gaussian ER Procrustes analysis find components with specific temporal shapes, each SCA step begins by finding the maximum amplitude across channels and time (instead of finding the maximum variance across the multichannel waveforms). First, the Gaussian function parameters (Eq. (1) and Fig. 1 bottom) are estimated with the *fit* Matlab function in the part of the waveform of the channel with maximum amplitude, on the time samples that are estimated to be valid with respect to the SNIR > 1 assumption, which is found by extending the time samples around the peak amplitude time sample until the nearest local minima or baseline crossing is reached. The SCA component waveform is modelled by applying the fitted function parameters. Since part of the data might contain non-Gaussian signals, if the Gaussian function parameter estimation fails, i.e., the errors between the modelled and measured data exceed the 95 % confidence intervals, the raw curve within the time samples is applied as a substitute instead of a modelled waveform, while the search for Gaussian shapes of lower amplitudes continues in the subsequent iterations.

Second, the component weighting matrix, $W_{n,c}$, for the weighting of each component waveform, n, on each channel, c, i.e. the topography of each component, is estimated with linear regression of each component waveform, x_n, on each residual channel waveform, y_c, based on the expression $y_c = W_{n,c}x_n$, with the Matlab function *mldivide*. To minimize the influence of false partial correlations between the component and channel waveforms, the linear regression is based on the complete range of time samples.

Third, the modelled component waveform is multiplied by the channel weight vector, $W_{n,c}$, to create a projection of the component waveform on the channels. Fourth, the component waveform projected back on the channels is subtracted from the multichannel waveforms to obtain the residual waveforms: $\varepsilon = y - Wx$, where ε is the residual waveforms, y is the measured waveforms, x is the modelled component waveforms, and W is the modelled channel weight vector.

The SCA procedure is performed, and components are estimated iteratively. The SCA procedure is based on minimizing the sum of the residual waveforms across channels and time, where the SCA procedure stops when the residual variance increases or reaches zero.

SCA based on Gaussian halves was performed using the same procedure with the *fit* function in Matlab, except that the parameters of one Gaussian function (Eq. (1)) was fitted to the part of the waveform leading up to the peak amplitude, and a second Gaussian function was fitted to the part of the waveform following after the peak amplitude. Also, SCA based on gamma functions was performed using the exact same procedure, and the parameters of the gamma function (Eq. (2)) were estimated with the *nlinfit* function in Matlab. SCA with sine functions was also achieved with the exact same procedure, although the parameters of the sine function (Eq. (3)) was fitted only to the sine half-wave with the *fit* Matlab function, and only the sine half-wave was applied in the back projection of the components onto the channel waveforms.

The Gaussian and sine models were available in the built-in curve fitting Matlab toolbox library models, and they were called 'gauss1' and 'sin1', respectively. Fit starting points for library models are by default determined heuristically. The toolbox selects new, random initial guesses for each function call. To our experience, the fitted coefficients remained the same across repeated tests of the same case indicating that the optimization is robust to differences in seed points.

The gamma model is not directly part of the available curve fitting Matlab toolbox library models, and the recommended gamfit Matlab function does not include the α coefficient, which corresponds to the amplitude parameter used in the Gaussian and sine models. Therefore, to match the gamma model with the Gaussian and sine models, it was necessary to use the *nlinfit* Matlab function, which allows a function handle, which here referred to the *gampdf* Matlab function (the same as applied in the recommended *gamfit* function), but with the α (amplitude) coefficient added to match the Gaussian and sine models. The initial guess of values for coefficients can only be set manually. Here we applied $k = 10$ as initial guess of the shape parameter for the component, because cases with $k \approx 10$ (mean $k \approx 8$) for regular cortical neurons were reported by Maimon and Assad (2009). Since the mean value of the gamma distribution, i.e., the mean latency, $\mu = k\theta$, and with $k = 10$, then $\mu = 10^*\theta$, and thus $\theta = 1/10^*\mu$. Therefore, the initial guess of θ was set to equal 1/10 of the observed peak latency, approximating $1/10^*\mu$. Also, for an initial guess of the α coefficient a value of 1/10 of the observed peak amplitude was applied. To our experience, initial guess values of $k < 10$ in general led to failure of the fitting algorithm, while other changes in the initial coefficient values *for α, k,* and θ did not appear to affect the resulting fitted gamma coefficients for the component. Generally, all fits terminated due to convergence (stopping criteria based on residual minimization).

2.4. Performance evaluation

The performance of the algorithms was evaluated with Pearson's product-moment correlation coefficients, r, between each modelled and measured single-subject ER. The explained variance was expressed as the mean r^2 across channels. In addition, the peak amplitudes (across the complete time range) were obtained from the residual waveforms, showing the peak amplitudes in the part of the waveform that could not be modelled by the SCA components (including any component substitutes with raw curves applied during the SCA procedure).

2.5. Statistical analysis

Statistical analyses were conducted with SPSS v. 25 (IBM, Armonk, New York, USA). The performance evaluations showed general tendencies towards high performances, resulting in skewed performance distributions diverging from normality in the positive direction (Kolmogorov-Smirnov and Shapiro-Wilk tests shows overall violations of the normality assumption at $p < .001$). Therefore, differences in performance, as defined in the preceding section, were tested with Friedman's ANOVA by ranks, and post hoc comparisons were conducted

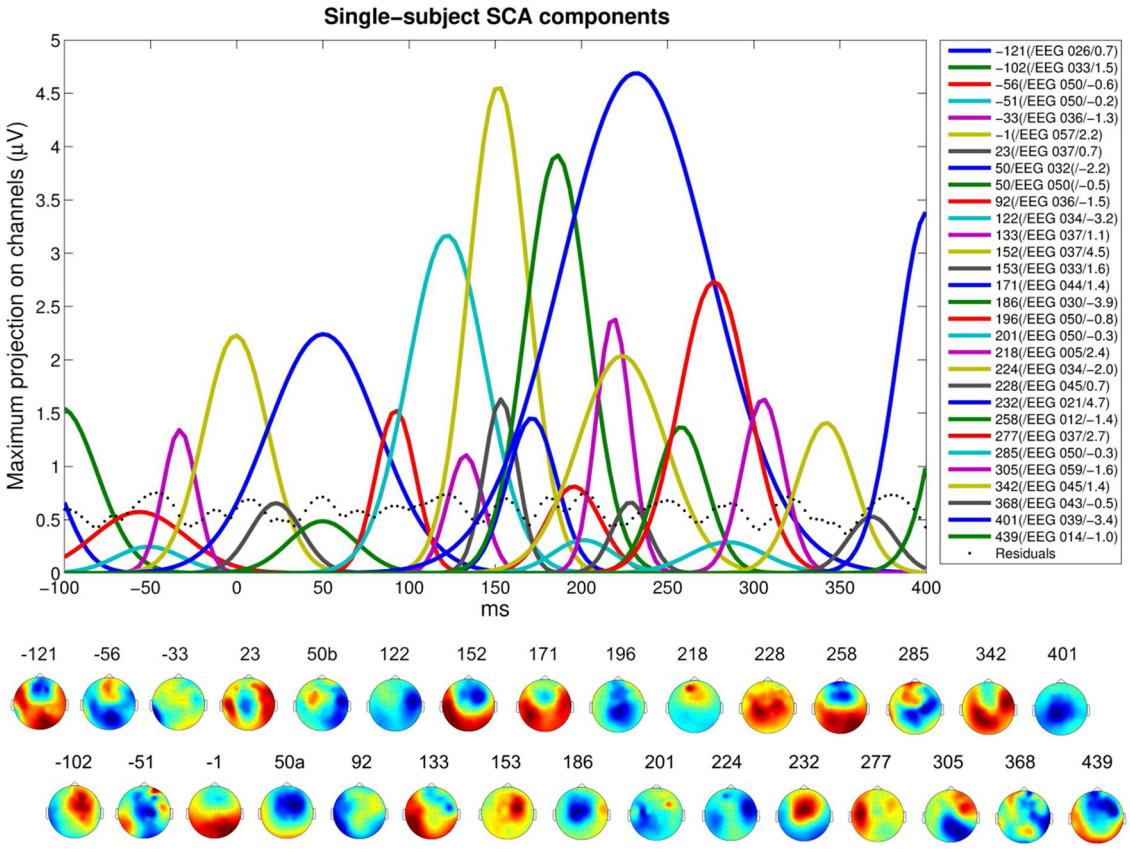

Fig. 2. An example of a single-subject evoked average waveform decomposed into SCA components. SCA components for a single-subject and stimulus condition (slide deviant) with the peristimulus time in ms on the horizontal axis and the EEG amplitude of the SCA components in the peak channel in μV on the vertical axis (irrespective of differences in peak channels across components). Below is shown the topographies of the components (color scales are set according to the maximum amplitude for each component). Numbers shown next to the component labels (right) and topographies (bottom) designate expected latency in ms. Component labels (right) are defined by expected latency in ms, name of peak channel, and amplitude (here in μV).

with Wilcoxon signed rank tests.

3. Results of study 1

An example of a typical result of an SCA decomposition with Gaussian functions is shown in Fig. 2.

Significant differences are observed in the percent explained variance of SCA with Gaussian functions compared to Gaussian halves, gamma or sine functions, $\chi^2(3) = 1519.29$, $p < < .001$ (Fig. 3A). Post hoc comparisons show that the Gaussian function describes the single-subject evoked average MEG/EEG waveforms significantly better than the Gaussian halves ($p < < .001$), gamma ($p < < .001$), and sine ($p < < .001$) functions (Fig. 3A and Table 2). Also, the Gaussian halves describes the MEG/EEG waveforms better than the gamma ($p < < .001$) and sine ($p < < .001$) functions, and the sine function describes the MEG/EEG waveforms slightly better than the gamma function ($p < .001$) (Fig. 3A and Table 2). In general, the SCA with the Gaussian function and Gaussian halves show gradual increases in the explained variance by the components, while the SCA modelled with gamma and sine functions fails explaining more variance after the first component estimate for the peak amplitude in the MEG/EEG waveform (Fig. 3B and Table 2). There is a relatively high variability in the number of Gaussian components explaining the individual M/EEG waveforms: median of 66 Gaussian components and a range between 4–160 Gaussian components (Table 2).

Across measurement modalities, the Gaussian function shows a slightly higher modelling performance on the average evoked responses from EEG waveforms compared to the MEG waveforms, while there is no significant difference in the Gaussian modelling performance on the MEG magnetometer and gradiometer waveforms (Fig. 3A–B and Table 2). Interestingly, the shape parameter, k, of the gamma function shows the highest median value for the EEG ($k = 45.7$) and lower values for the MEG magnetometers ($k = 34.1$) and MEG gradiometers ($k = 34.7$), $\chi^2(2) = 19.51$, $p < 10^{-4}$, indicating lower skewness ($\Upsilon = 2/\sqrt{k}$) in the EEG (Υ(EEG) = .30) compared to the MEG (Υ(MEG mag.) = .34; Υ(MEG grad.) = .34) measurement modality.

There is significant decrease in the modelling performance with Gaussian functions on the evoked average MEG/EEG waveforms that have not been preprocessed compared to those that have been preprocessed, $p < < .001$ (Fig. 3C). Also, the peak amplitudes in the residual waveforms is larger for the Gaussian SCA models without preprocessing compared to with preprocessing in the EEG, $p < < .001$, MEG magnetometers, $p < < .001$, and MEG gradiometers, $p < < .001$ (Fig. 3D–F). The same decrease in performance for unprocessed compared to preprocessed MEG/EEG waveforms is observed for SCA based on Gaussian halves, $p < < .001$, gamma, $p < < .001$, and sine, $p < < .001$, functions. Similarly, peak amplitudes in residual waveforms are larger without preprocessing compared to with preprocessing for the Gaussian halves based SCA, in the EEG, $p < < .001$, MEG magnetometers, $p < < .001$, and MEG gradiometers, $p < < .001$, for the gamma-based SCA, in the EEG, $p < < .001$, MEG magnetometers, $p < < .001$, and MEG gradiometers, $p < < .001$, and for the sine-based SCA, in the EEG, $p < < .001$, MEG magnetometers, $p < < .001$, and MEG gradiometers, $p < < .001$ (Fig. 3D-F). The grand average waveforms obtained with all the compared methods are shown in Fig. 4.

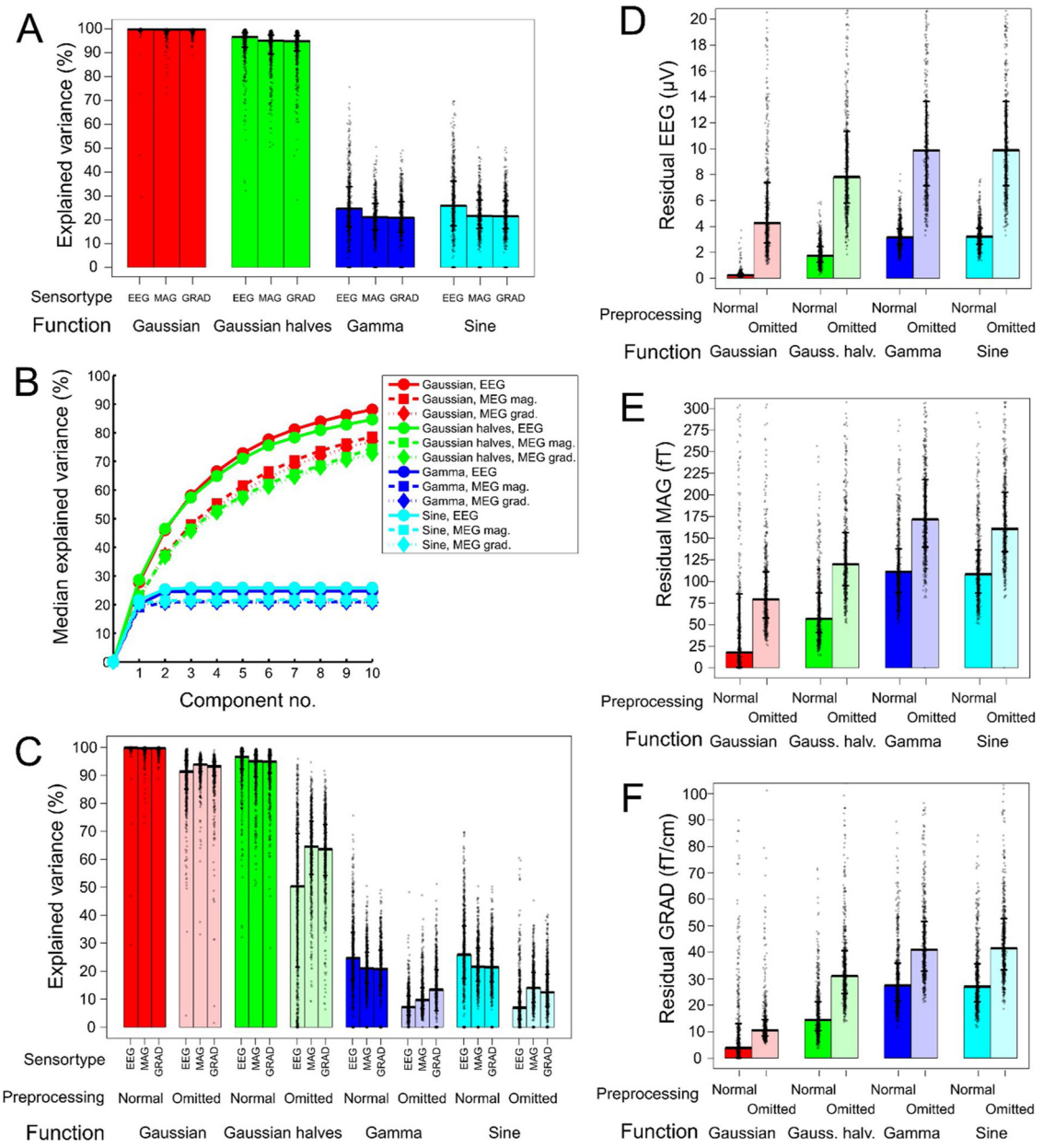

Fig. 3. The variance in the single-subject average evoked MEG/EEG waveforms is more accurately explained by the Gaussian components (shown in red) compared to the Gaussian halves (green), gamma (blue) and sine (cyan) components (*A*). (MAG: MEG magnetometers; GRAD: MEG gradiometers. Bars designate medians and error bars indicate interquartile ranges.) Also, the cumulative percent of variance explained by the first ten components (in descending order of amplitude) shows an early onset of the higher accuracy of the Gaussian function during the MEG/EEG waveform decomposition (*B*). When MEG/EEG preprocessing (for removing artifactual signals not originating from the brain) is omitted (shown in brighter colors), a reduction in the accuracy of the SCA functions is seen (*C*), and higher peak amplitudes remain in the residual EEG (*D*), MEG magnetometer (*E*) and gradiometer (*F*) waveforms after the decomposition into SCA components. (For interpretation of the references to colour in this figure legend, the reader is referred to the web version of this article.)

4. Interim discussion 1

The findings in the first study support our hypothesis that large-scale spike density components in MEG/EEG waveforms originating from neural networks can accurately be described by Gaussian functions, with median 99.7 %–99.9 % of the variance explained by Gaussian functions. The single-subject average evoked responses MEG/EEG waveforms could also to some extent be modelled with Gaussian halves, however, with lower performance in comparison to the symmetric Gaussian functions. While the first component, of highest amplitude, to some extent could be approximated by gamma and sine functions, our findings suggest that the Gaussian function more accurately models the complete set of spike density components in the single-subject average evoked responses MEG/EEG waveforms. It seems unlikely that the high performance of the Gaussian function is related to the high pass and low pass filter response, because the filter has a constant response shape, while the modelled Gaussian components vary in width, and the performance of the Gaussian function is still relatively high without the preprocessing, i.e., with filtering excluded. As with any MEG/EEG analysis in general, with the SCA method it is necessary to consider a compromise between the suppression of artifactual signals while retaining as much of the component of interest across frequency bands. In addition, it is unlikely that the Gaussian distribution is caused by timing error in the signal averaging across trials, because the component of interest in the single-trial evoked responses is typically identical in shape with the average single-subject waveform when the

Table 2
Percent explained variance by Gaussian, Gaussian halves, gamma, and sine functions. Post hoc comparisons for percent explained variance in EEG, MEG magnetometer (MAG), and MEG gradiometer (GRAD) after decomposing the single-subject evoked responses into Gaussian, Gaussian halves, gamma, and sine components. Showing median percent explained variance and median number of SCA components. Ranges are shown in parenthesis.

		% explained variance (range)	Post hoc comparisons, *p*, for % explained variance		Number of SCA components (range)
SCA function	Modality		EEG	MEG mag.	
Gaussian	EEG	99.9 (29.3–100.0)	–	–	69 (4–154)
	MEG mag.	99.7 (72.9–100.0)	< < .001 *	–	62 (10–160)
	MEG grad.	99.7 (88.8–100.0)	< < .001 *	.265	65 (20–153)
Gaussian halves	EEG	96.6 (32.1–99.9)	–	–	59 (3–72)
	MEG mag.	95.1 (50.6–99.5)	–	–	58 (19–72)
	MEG grad.	94.9 (28.3–99.4)	–	–	59 (7–76)
Gamma	EEG	24.7 (0.0–75.6)	–	–	1 (0–1)
	MEG mag.	21.0 (0.0–50.5)	–	–	1 (0–1)
	MEG grad.	20.8 (0.0–49.0)	–	–	1 (0–1)
Sine	EEG	25.9 (0.0–69.7)	–	–	1 (0–1)
	MEG mag.	21.6 (0.0–50.3)	–	–	1 (0–1)
	MEG grad.	21.4 (0.0–50.2)	–	–	1 (0–1)

stimulus condition remains constant (Gaspar et al., 2011). Moreover, while the current sources of the spike density might be considered to move in space as they propagate on the cortex, findings from research on 'micro-states' suggests that the component topography does not change significantly across time except in the transitions between components (Koenig et al., 2014; Lehmann, 1989; Pascualmarqui et al., 1995), which supports the validity of applying constant channel (*c*) weights, $W_{n,c}$, for each component (*n*). The overlap between components when their relative amplitudes change will result in topographies that through visual inspection appear to be moving across time, even

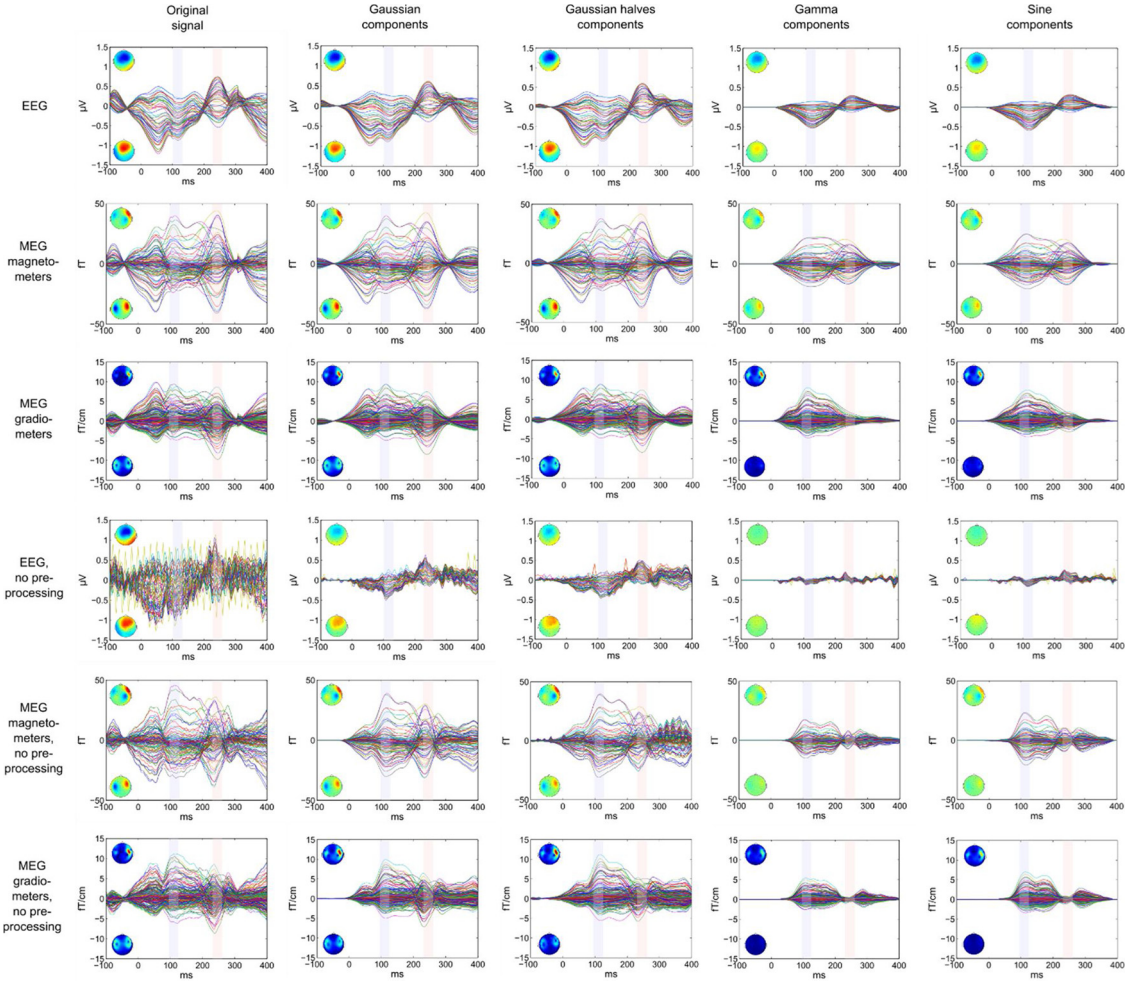

Fig. 4. Components extracted with Gaussian, Gaussian halves, gamma, and sine functions across all cases. Showing the grand-average butterfly waveform plots for the extracted first five SCA components across all 564 cases. The topography is shown next to each waveform by using a 30 ms time window around the peak latencies of the negative component (MMN) marked with a light blue rectangle (peak latencies: EEG = 116 ms, MEG magnetometers = 113 ms, MEG gradiometers = 110 ms) and the positive component (P3a) marked with a light red rectangle (peak latencies: EEG = 243 ms, MEG magnetometers = 245 ms, MEG gradiometers = 246 ms). (For interpretation of the references to colour in this figure legend, the reader is referred to the web version of this article.)

though the topography of each separate component might be relatively constant.

Our findings also showed that the skewness reflected by the fitted gamma shape parameter was lower for EEG compared to MEG. The high performance of the fitted symmetric Gaussian functions and the low performance and higher skewness in the MEG than the EEG with fitted gamma functions might suggest that partial overlap of latent symmetric Gaussian components results in more skewed waveform shapes in the MEG than the EEG. This might reflect that the signal gain in the measurement angle of the EEG electrodes causes less overlap between, e.g., the MMN and P3a responses of opposite polarities, while such overlap might have stronger influence on the signal gain of the MEG magnetometer and gradiometer sensors. Another explanation could be that the higher skewness and the slightly lower percent explained variance in MEG compared to EEG is related to general differences in the spatial specificity affecting how much of the complete spiking distribution is included in the measurements. The measured part of the large-scale spike timing distribution in a neural assembly might be most complete and thus most symmetrically distributed in the largest-scale EEG measurements, less complete and thus more skewed in the more spatially specific MEG magnetometers and gradiometers, and most incomplete in the highly spatially specific intracranial measurements that show the highest skewness in the measured spike timing distribution (Maimon and Assad, 2009).

While the findings in Study 1 suggests that MEG/EEG waveforms can accurately be decomposed into spike density components with the SCA method, in the following Study 2, we investigated whether the SCA method can be applied to isolate a specific evoked response of interest from spatially and temporally overlapping neural sources with higher accuracy compared to PCA and ICA.

5. Materials and methods for study 2

5.1. Repository dataset

The repository dataset for Study 2 was the exact same as in Study 1.

5.2. SCA, ICA and PCA decomposition

The SCA decompositions were performed following the same procedure as in Study 1. The SCA results were compared with those of principal component analysis (PCA) and independent component analysis (ICA).

The PCA decomposition was performed by applying the *varimax* Matlab function from the EEGLab Toolbox (Delorme and Makeig, 2004) referred by the FieldTrip Toolbox. PCA is an iterative procedure by which the waveform explaining most of the variance in the data is estimated and subtracted from the data, while subsequent components explaining most of the remaining variance in the data are repeatedly estimated (Jung et al., 1998). A constraint is imposed that each weaker component must be topographically orthogonal to the preceding component, in order to increase spatial independence between the components (Jung et al., 1998). The PCA was calculated based on the cross-covariance matrix and by applying the orthogonal Varimax rotation, which maximizes the variance of the squared loadings of each component (Kaiser, 1958). While orthogonal PCA typically succeeds suppressing the signal of spatially dissimilar components explaining less variance from components explaining more variance, it fails in separating mixed signals from spatially similar components (Jung et al., 1998). Also, oblique PCA rotation, which allows components to be partially correlated, such as Promax rotation, has been tested on simulated EEG data. However, while we here focus on spatial component analysis, the most reliable findings with oblique PCA have mainly been observed with temporal PCA, where constant temporal shapes are estimated by applying Promax rotation on a constrained PCA subspace derived from simulated EEG data (Dien, 2010).

ICA achieves higher spatial accuracy than PCA by separating the mixed multichannel signals into spatially statistically independent sources across time (Groppe et al., 2008). However, weaknesses of ICA concern its dependency on estimating the projection weights based on statistics obtained across time, whereby its accuracy decreases with lower SNR (related to higher background noise) (Comon, 1994) and fewer time samples (Jung et al., 2000). Therefore, ICA is able to isolate, e.g., eye blink artifactual components accurately, because they exhibit high SNR and can be estimated based on several time samples in the continuous MEG/EEG recording (Haumann et al., 2016). However, the assumptions underlying ICA are violated for brain responses that show either low SNR in the continuous recording, or few time samples if signal averaging is applied to increase the SNR. Therefore, the evoked response waveforms are likely to be distorted when ICA is applied to decompose these signals (Groppe et al., 2008). Also, if ICA components are estimated from concatenated averages of MEG/EEG signal across experimental conditions and subjects, one obtains summary statistics that ignores the individual variance across conditions, which compromises the single-subject analysis (Groppe et al., 2008).

The ICA decomposition was performed with the Infomax algorithm, implemented in the *runica* function for Matlab, which has been shown to be among the most accurate ICA algorithms for EEG data (Crespo-Garcia et al., 2008; Delorme et al., 2007) and is also commonly applied for artifact correction for MEG and EEG data (Haumann et al., 2016). First, the rank of the average ER waveform was estimated with the *rank* Matlab function. The resulting rank number was given as input to the *runica* function for the initial PCA-based dimensionality reduction step prior to the ICA procedure. In cases where the ICA decomposition resulted in imaginary numbers in the component waveforms or topographies, due to overestimates of the rank, the assumed rank and PCA-based dimensionality output was reduced by 1, and the ICA decomposition repeated, until the resulting ICA estimates contained only real numbers.

5.3. Automatic component of interest extraction based on template match

The stimulus paradigm was specifically designed to evoke MMN responses, and the investigated dataset contained a total of 1692 cases of averaged MEG/EEG multichannel waveforms with MMN responses to be analyzed (564 cases simultaneously recorded with EEG, MEG magnetometers, and MEG gradiometers). Since each case was analyzed with SCA, ICA, and PCA, the resulting set of 5076 decompositions in total was relatively large for conventional manual MMN identification and extraction. Moreover, it was important to ensure that the MMN components were extracted following the exact same procedure across the SCA, ICA, and PCA decompositions. Therefore, an automatic extraction procedure was developed, which was based on a template matching approach (for similar automation methods, see (Lee et al., 2003) and (Armanfard et al., 2018)). Since the dataset contained six different types of deviant stimuli affecting the MMN component, all MMN components were identified separately for each type of deviant stimulus. The group-level average of the individual ERs more closely approximates the true topography and waveform morphology of the component of interest than the individual ERs, because the group-level waveform has a higher signal-to-interference and noise ratio than the single-subject averaged waveforms (Dien et al., 2007; Luck, 2014). Therefore, the grand average group-level MEG/EEG waveforms were applied as templates (Lee et al., 2003) and matched against the SCA, ICA, and PCA components.

There is no automatic standard approach to extract an MEG/EEG component of interest from component analysis (e.g., PCAs or ICAs). However, in the manual standard approach an expert determines by visual inspection whether components in the decomposition matches the typical topography and common waveform morphology of the component of interest within reliable time points (Jung et al., 1998; Luck, 2014):

1 Following the manual standard approach, reliable time points, t_{comp}, containing the MMN component waveform in the group-level template were isolated by finding the peak amplitude and extending the selected time points around the peak until they reach the baseline value at 0. In addition, the t_{comp} was constrained to be within the typical MMN component range of 75 − 250 ms (Näätänen et al., 2019).
2 In the manual standard procedure, the component topography is matched with a typical component topography (Jung et al., 1998), i.e., a common scalp distribution (e.g., for an EEG MMN component a frontal negativity at Fz and positivity at mastoids). Matches between components and group-level templates were implemented in terms of Pearson's correlation *r*-estimates. The match in component topography was expressed in *r*-values, r_{topo}, by correlating each component topography with the average group-level topography across the time window t_{comp}.
3 According to the manual standard procedure the component waveform morphology is matched with a typical waveform morphology to find a deflection in the normal latency range (or frequency band) (Jung et al., 1998) (e.g., for an MMN component a deflection with an increase, peak, and decrease in the 75 − 250 ms latency range). The component waveform matches expressed in *r*-values, r_{wave}, were estimated by correlating each component waveform projection on each channel with the group-level waveform for the channel, and applying the mean *r*-value across the channels in the time window t_{comp}.
4 Next, following the standard procedure of combining the match in topography and waveform morphology (Jung et al., 1998) a combined R^2-value was defined as: $R^2 = r_{topo} \times r_{wave}$, where components were taken into subsequent consideration if both r_{topo} and r_{wave} were positive values (excluding invalid cases of anticorrelations). For each SCA, ICA, and PCA decomposition, the single-subject components were sorted in descending order according to their resulting R^2-values indicating their match with the group-level template.
5 Finally, the component of interest can be composed of more sub-components in the decomposition (Jung et al., 1998; Luck, 2014). Therefore, following the order of the R^2-values (highest to lowest), each component was projected and summed into the extracted channel waveforms, as long as the addition of a component resulted in an increase in the correlation, *r*, which was initially set to $r = 0$. The correlation, *r,* was calculated by correlating the projected component waveform with the group-level waveform in the time window t_{comp} and obtaining the mean *r* across channels. Thereby, 0 or more sub-components matching the MMN topography and waveform morphology were automatically extracted from the SCA, ICA, and PCA decompositions.

5.4. Performance calculations

The accuracy of the SCA, ICA, PCA methods for decomposing MMN components and the accuracy of the original MEG/EEG waveforms in representing the MMN components was evaluated and compared. First, the ability to remove interfering signals was evaluated by calculating the root-mean-squared error between the ideal baseline with values of 0 and the waveform values outside the MMN time range t_{comp}. Also, the group-level topography and waveform morphology have higher SNIR, because it is based on a signal averaging across more trials compared to the individual averages, and thereby approximates the true topography and waveform morphology more than the individual averages (Dien et al., 2007; Luck, 2014). Therefore, it is relevant also to benchmark the individual topographies and waveform morphologies for the SCA, ICA, PCA and original results by correlating them with the group-level topography and waveform morphology. The accuracy of the MMN topography was calculated as the r^2-value based on the squared correlation coefficient between the extracted MMN component topography and the group-level MMN topography within the time points t_{comp}. Also, the accuracy of the MMN waveform was calculated as the mean r^2-value equal to the mean squared correlations coefficients between the extracted single-subject MMN waveform and the group-level MMN waveform across channels within the time points t_{comp}. Also, the number of sub-components representing the MMN with SCA, ICA, and PCA was counted.

5.5. Statistical analysis

Since the performance values were not normally distributed (most Kolmogorov-Smirnov and Shapiro-Wilk test results are $p < .001$), differences in performance were, as in Study 1, tested with Friedman's ANOVA by ranks, and post hoc comparisons were conducted with Wilcoxon signed rank tests.

6. Results of study 2

The SCA method showed a significantly higher performance in removing the interfering signals overlapping with the individual MMN responses than the ICA and PCA methods with respect to the EEG, $\chi^2(3) = 1099.50$, $p < < .001$, MEG magnetometers, $\chi^2(3) = 1117.01$, $p < < .001$, and gradiometers, $\chi^2(3) = 1138.51$, $p < < .001$ (Fig. 5A-C and Table 3). The best removal of interfering signals was achieved with the SCA, followed by the ICA, and PCA. The resulting grand averages of the MMN topographies and waveforms achieved with each component analysis method are shown in Fig. 6.

The similarity of the single-subject and group MMN topography differed significantly between SCA, ICA, PCA, and the original, $\chi^2(3) = 178.08$, $p < < .001$ (Fig. 5D). All component analysis methods resulted in representations of the MMN topography that were more similar to the group-level topography compared to the original individual topographies (Fig. 5D and Table 4). There was a slightly higher similarity between the component and group-level topographies for ICA compared to SCA and PCA, and for SCA compared to PCA (Fig. 5D and Table 4). Moreover, the MMN topography was more similar between the group-level and individual SCA topography for the EEG than for the MEG magnetometers ($p < < .001$) and MEG gradiometers ($p < < .001$), while no significant difference was observed between the MEG magnetometers and gradiometers ($p = .066$) (Fig. 5D).

The similarity between the single-subject and group MMN waveforms also differed significantly depending on the applied method, $\chi^2(3) = 434.69$, $p < < .001$ (Fig. 5E). The extracted single-subject SCA and PCA components showed higher similarity with the group-level MMN waveforms compared to the ICA components and original single-subject waveforms (Fig. 6 and Table 4). There was no significant difference in resemblance with the group-level MMN waveforms for the SCA components compared to the PCA components. However, the representation of the MMN waveform with the ICA components was worse than the original single-subject waveforms (Fig. 5E and Table 4). There was a minor decrease in the similarity between the group-level MMN waveform and individual SCA waveforms for the MEG magnetometers compared to the EEG ($p < .001$) and MEG gradiometers ($p < < .001$), while no difference in similarity of the group-level and individual SCA waveforms was observed for the EEG and the MEG gradiometers ($p = .350$).

We also observed a minor difference in the number of estimated components extracted from the SCA, ICA, and PCA decompositions representing the MMN, $\chi^2(2) = 15.65$, $p < .001$ (Fig. 5F). In general the MMN is estimated to be represented by one component, however, post hoc comparisons suggested that there was a tendency of more estimated components representing the MMN in the ICA compared to the SCA decompositions ($p = .003$), while SCA and PCA ($p = .052$) and ICA and PCA ($p = .157$) decompositions tended to contain similar numbers of estimated components representing the MMN. The SCA decompositions contained slightly different numbers of estimated components representing the MMN dependent on the measurement

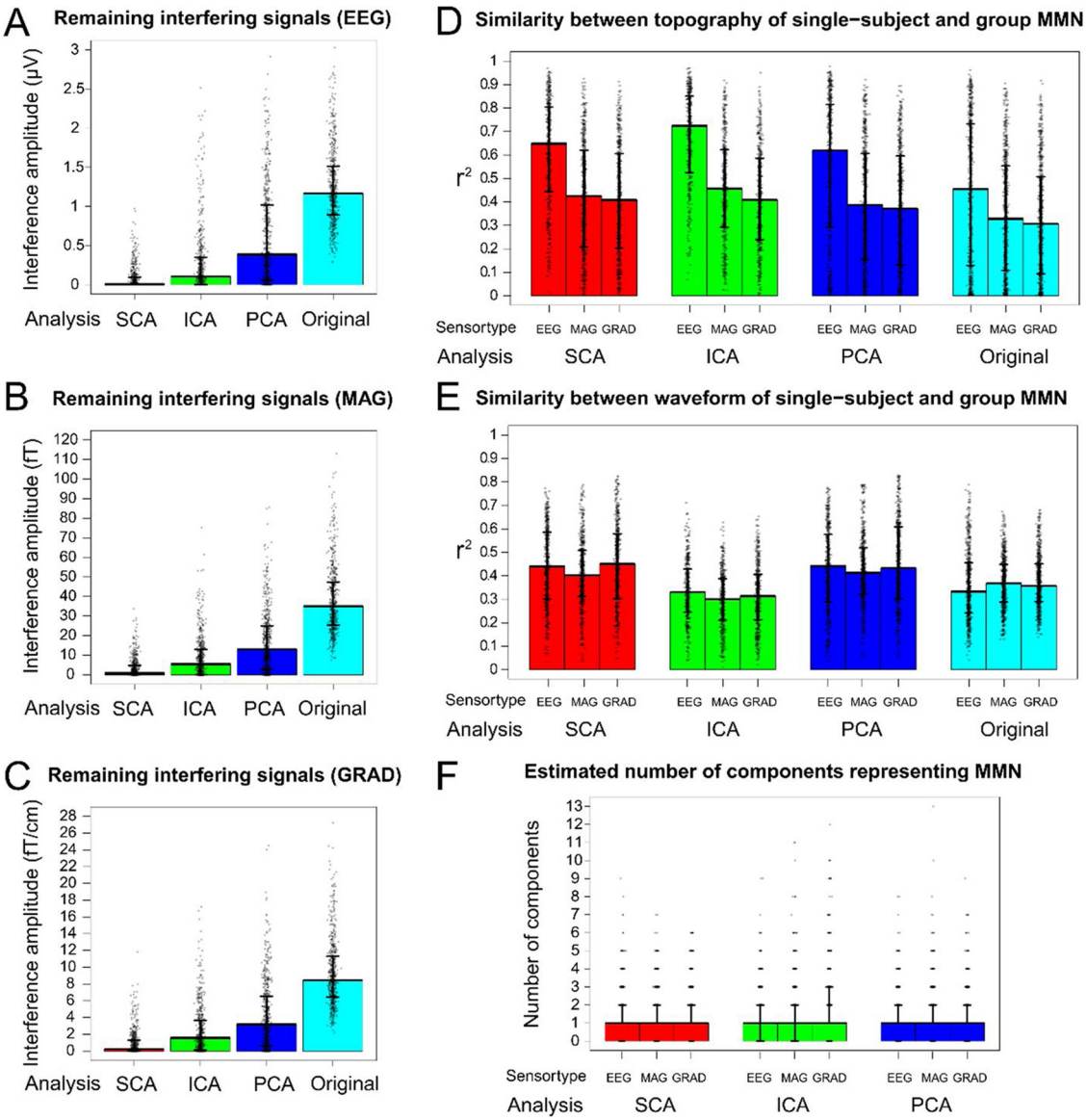

Fig. 5. The SCA analysis suppresses the interfering signals significantly more in the EEG (*A*), MEG magnetometer (*B*) and MEG gradiometer (*C*) in comparison to the ICA and PCA analyses and the original evoked single-subject waveforms. (Results are shown for SCA in red, for ICA in green, for PCA in blue, and for original single-subject averages in cyan. MAG = MEG magnetometers; GRAD = MEG gradiometers. Bars designate medians and error bars indicate interquartile ranges.). Generally, the component analyses result in topographies with higher similarity to the MMN group-level topography compared to the original single-subject average evoked response topography (*D*). Specifically, the extracted SCA and PCA waveforms more closely resembles the group-level waveform in comparison to the ICA and original individual waveforms (*C*). Finally, the single-subject SCA analysis provides the most sparse representation of the MMN response in terms of number of estimated components representing the MMN (*F*). (For interpretation of the references to colour in this figure legend, the reader is referred to the web version of this article.)

modality, $\chi^2(2) = 7.81$, $p = .020$ (Fig. 5F). The SCA decompositions of the EEG waveforms contained slightly more estimated components representing the MMN compared to those for the MEG gradiometer waveforms ($p = .001$), while there were no differences between EEG and MEG magnetometer waveforms ($p = .063$) and MEG magnetometer and gradiometer waveforms ($p = .054$).

7. Interim discussion 2

The results of Study 2 show as hypothesized that the novel SCA decomposition method accurately isolates an evoked response of interest, in this case the MMN, from other interfering neural sources in the single-subject evoked average MEG and EEG waveforms. In terms of the accuracy in the isolation of the evoked response of interest, the SCA method clearly outperforms the ICA and PCA methods. Also, the findings show that the evoked response of interest is more accurately represented in the extracted SCA components than in the original measurements. Moreover, as expected, the ICA decompositions suffered in particular from non-veridical reproduction of the MEG/EEG waveforms. Furthermore, as expected, the PCA components were only partially separated, with interfering signals partially mixed with the component of interest in the PCA decomposition.

The slightly higher resemblance between the grand average and individual PCA waveforms compared to the similarity of the grand average and individual SCA waveforms does not necessarily indicate a more precise extraction of the MMN response with PCA. The relatively high resemblance between the original and PCA waveforms could be explained by a mutual failure in suppressing the overlapping P3a response. Fig. 6 supports this assumption, since in both the original waveforms and the PCA waveforms the negative MMN amplitude appears lower than in the SCA waveforms, and also the zero-crossings (~200 ms) and the peak of the positive P3a response (~250 ms) are

Table 3
Remaining interfering signals overlapping with component isolated with SCA, ICA, and PCA. Post hoc comparisons for the root-mean-squared error (RMSE) from a perfect MEG/EEG waveform baseline of values 0 in the time range surrounding the component of interest, t_{comp}, for EEG, MEG magnetometer (MAG) and MEG gradiometer (GRAD) waveforms when applying SCA, ICA, PCA or the original waveforms.

Remaining interfering signals (EEG)				
Method	Median μV	Post hoc comparisons, *p*		
SCA	0.005	SCA	ICA	PCA
ICA	0.103	< < .001 *		
PCA	0.385	< < .001 *	< < .001 *	
Original	1.165	< < .001 *	< < .001 *	< < .001 *
Remaining interfering signals (MAG)				
Method	Median fT	Post hoc comparisons, *p*		
SCA	0.819	SCA	ICA	PCA
ICA	5.395	< < .001 *		
PCA	13.056	< < .001 *	< < .001 *	
Original	35.044	< < .001 *	< < .001 *	< < .001 *
Remaining interfering signals (GRAD)				
Method	Median fT/cm	Post hoc comparisons, *p*		
SCA	0.241	SCA	ICA	PCA
ICA	1.579	< < .001 *		
PCA	3.185	< < .001 *	< < .001 *	
Original	8.442	< < .001 *	< < .001 *	< < .001 *

present in the original and PCA waveforms, whereas, as expected, the positive P3a response seems absent in the SCA waveforms.

While Study 1 and Study 2 showed that the SCA method can be applied to isolate a specific component of interest in single-subject evoked responses, it remains to be verified whether SCA is a reliable method for the study of inter-individual differences measurable in a specific component. In particular, we tested whether the previous findings of increased MMN amplitude to pitch and slide deviants measured in the MEG gradiometers in subjects with higher traits of depression (Bonetti et al., 2017) could be replicated with the SCA method.

8. Materials and methods for study 3

8.1. Repository dataset

For Study 3 the same dataset was applied as in Study 1 and Study 2 and in a previously reported study on effects of depressive traits on MMN (Bonetti et al., 2017). The study included a subset of 75 subjects rated on the Montgomery–Åsberg Depression Rating Scale (MADRS) (Bonetti et al., 2017).

The measured MMN components were categorized according to six types of auditory deviants that evoked the MMN: 1) intensity deviants with −6 dB change in sound amplitude, 2) location deviants where the sound amplitude in one of the stereo sound channels was lowered, 3) rhythm deviants with shortening of a tone by 60 ms, 4) pitch deviants with 1.4 % change in tone frequency, 5) slide deviants with gradual change in tone frequency, and 6) timbre deviants with an "old time radio" sound spectrum filter-effect (Bonetti et al., 2017).

8.2. Statistical analysis

The mean amplitude was measured in a 30-ms time window centered on the peak latency in the grand average, measured separately for each deviant type. As in the previous study the effect was investigated for the MEG gradiometers (Bonetti et al., 2017), and the combined gradiometer channels MEG 1322 + 1323 above the right hemisphere which showed the largest amplitude was applied for testing with linear regression. Statistical test results were obtained with linear regressions between the MADRS score and the extracted mean MMN amplitude for each type of deviant.

9. Results of study 3

The same effects of individual depression trait on the MMN amplitudes for the spectral features were observed in both the original data and in the MMN components extracted with the SCA method (Fig. 7 and Table 5). Increasing depression scores were related to increasing MMN amplitudes in response to spectral changes (pitch, slide, and timbre) in acoustic features of the sound stimulation. Also, the effects where replicated for the MMN components extracted with ICA and PCA, however, with smaller effect sizes (Table 5) and less consistent waveforms (Fig. 7) compared to the MMN components extracted with SCA.

10. Interim discussion 3

The findings of Study 3 show that inter-individual differences in MMN amplitudes are preserved when the individual MMN responses are extracted with the SCA method. However, the true individual MMN responses are unknown in the empirical MEG/EEG. Therefore, in the following study we simulate MMN responses, interferences, and noise, and test how much the simulated MMN responses with interference and noise extracted with the SCA, ICA, and PCA methods diverge from the true simulated MMN responses.

11. Materials and methods for study 4

11.1. Simulation of controlled realistic Gaussian signals, interferences, and noise

MMN signals and P3a interferences were simulated based on realistic empirical responses to three auditory spectral deviants (pitch, slide, and timbre deviants). The SCA method was applied to fit Gaussian function parameters and channel weights to the empirical MMN and P3a grand average responses from the dataset applied also in Studies 1–3. The modelled realistic MMN responses were applied for the simulated MMN signals and the P3a responses for interferences. Also, realistic empirical alpha wave interferences were simulated by applying the SCA method to derive an alpha half-wave cycle. Based on the Gaussian function parameters, a regular time series of Gaussian-shaped alpha half-waves were simulated at different latencies to imitate realistic alpha waves at a realistic frequency of 10 Hz. Finally, white noise was simulated with the *randn* Matlab function. The simulated MMN, P3a, alpha, and noise waveforms are illustrated in Fig. 8.

EEG MMN waveforms were simulated at amplitude values 0.50–5.00 μV with a step-size of 0.50 μV, P3a waveforms at amplitude values 0.50–10.00 μV with a step-size of 0.50 μV, and alpha waveforms at amplitude values 0.25–5.00 μV with a step-size of 0.25 μV. A constant EEG noise amplitude value of 0.5 μV was applied. The noise was pre-processed with a 1 Hz high-pass and 25 Hz low-pass filter by following the same procedure as in the empirical MMN studies (1 s extra noise for filter padding was added before and after the final applied noise segment to avoid filter distortion at the edges of the noise segment). The average filtered noise across 100 trials was applied in the simulation. The amplitudes for each MMN, P3a, and alpha waveform were tested in each possible combination, which resulted in 4000 waveforms (each with 60 channels and 151 time points) with tested amplitude combinations for each of the pitch, slide, and timbre deviant responses (Fig. 8A).

The simulated MMN signals and alpha and P3a interferences were weighted by their channel weights obtained from the empirical grand averages using the SCA method (Fig. 8B). A constant weight was

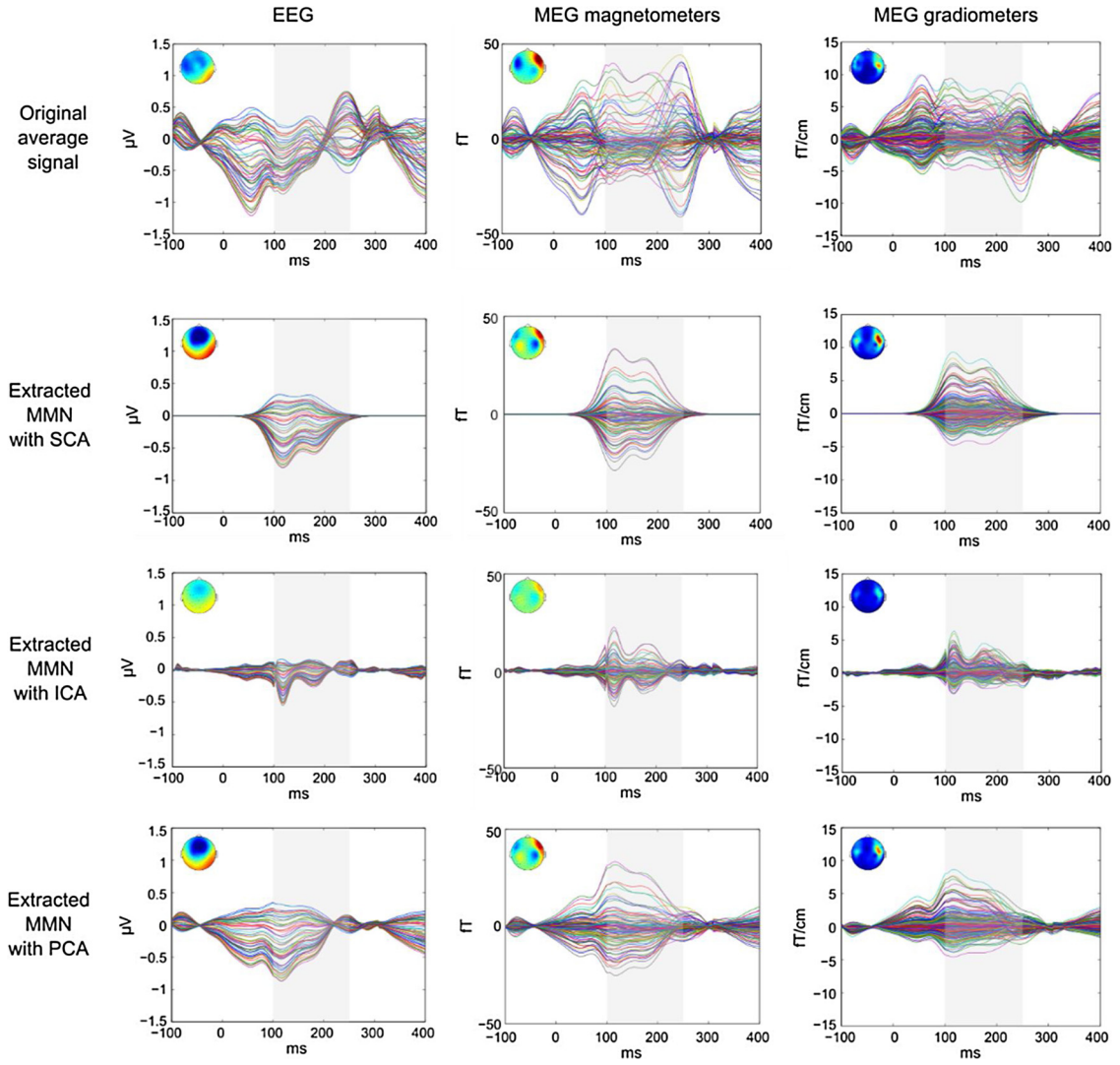

Fig. 6. MMN extracted with SCA, ICA and PCA. The top row shows the butterfly waveforms for the original average signal for EEG (left), MEG mag. (middle), and MEG grad. (right), the second row shows the same for SCA, the third row for ICA, and the fourth row for PCA. Next to each waveform the signal topography is shown in the component of interest time range, t_{comp}.

Table 4
Similarity of topography and waveform between single-subject and group MMN. Post hoc comparisons on topography and waveform similarities for EEG, MEG magnetometer (MAG) and MEG gradiometer (GRAD) waveforms applying SCA, ICA, PCA or the original single-subject average waveforms.

Similarity between topography of single-subject and group MMN

Method	Median r^2	Post hoc comparisons, p		
SCA	.44	SCA	ICA	PCA
ICA	.49	< < .001 *		
PCA	.41	< < .001 *	< < .001 *	
Original	.36	< < .001 *	< < .001 *	< < .001 *

Similarity between waveform of single-subject and group MMN

Method	Median r^2	Post hoc comparisons, p		
SCA	.42	SCA	ICA	PCA
ICA	.32	< < .001 *		
PCA	.42	.345	< < .001 *	
Original	.36	< < .001 *	< < .001 *	< < .001 *

applied for a single noise waveform uniformly present on all simulated channels.

Finally, the simulated MMN signal, alpha and P3a interference, and noise waveforms were mixed by summing their waveforms (Fig. 8C). The SCA, ICA, and PCA methods were mainly challenged by interference between the MMN and alpha wave. The alpha interference pattern was constructive for the pitch and slide MMN and destructive for the timbre MMN. Also, there was destructive interference patterns between the alpha waves and the pitch and slide P3a, which cancel out interference on the pitch and slide MMN.

11.2. Simulation of approximated real signals, interferences, and noise

The controlled simulation with Gaussian signals and interferences was based on the assumption that the neural signals measured with EEG/MEG have Gaussian temporal shapes, which was supported by the findings in Study 1. Also, we included an additional simulation that did not require this assumption to be true. The additional simulation was based on real single-subject EEG waveforms, and the true MMN signal was approximated with regression methods. In comparison to the controlled simulation the manipulations of real EEG waveforms make this additional simulation more realistic, however, since the approximated true signals partially contains interference and noise, the results

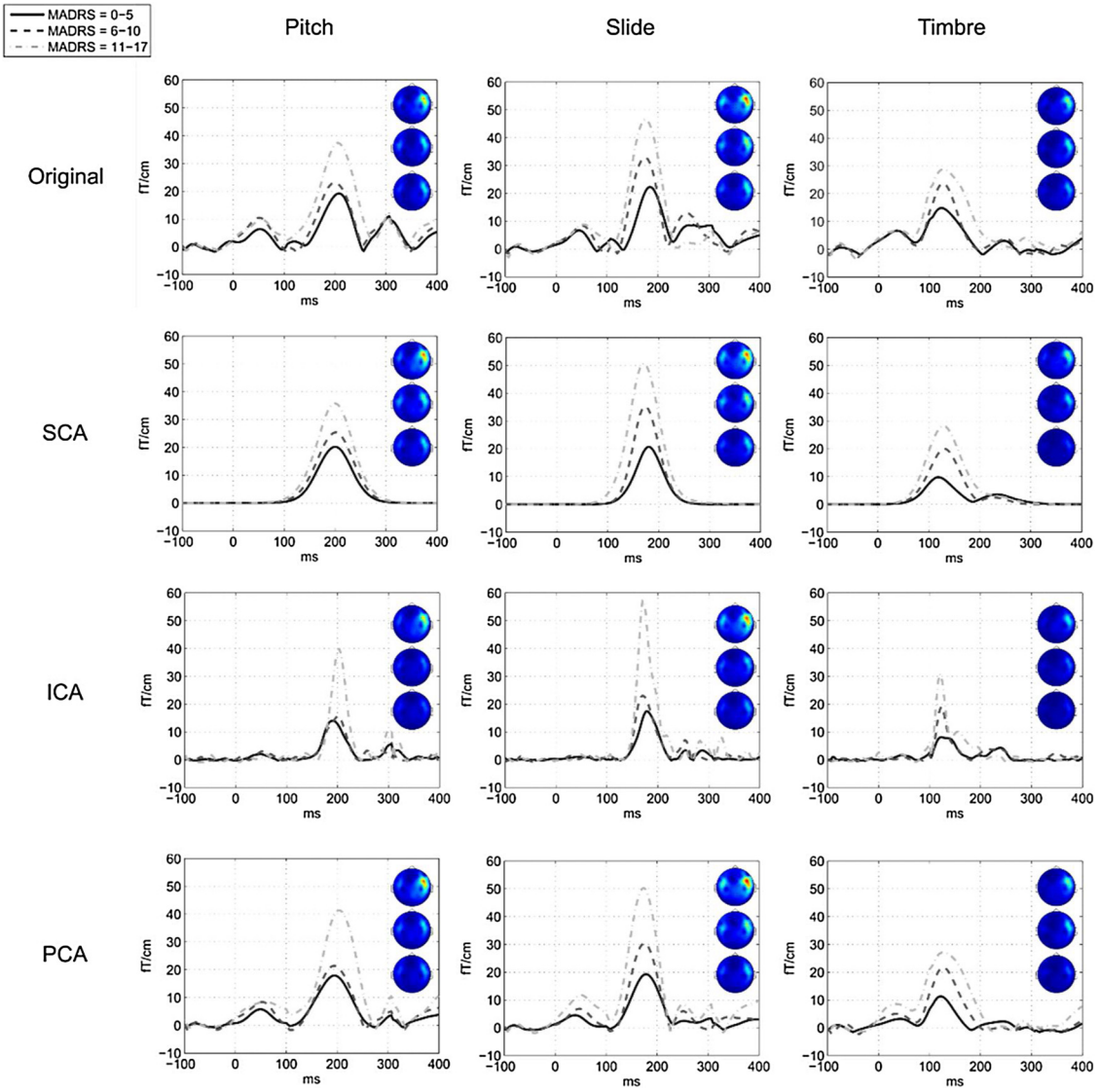

Fig. 7. Average MEG gradiometer waveforms and topographies of single-subject MMN responses to pitch, slide, and timbre deviants extracted with SCA, ICA, and PCA for subjects with low (0–5), medium (6–10) and high (11–17) depression scores (MADRS). (Additional waveforms and topographies for EEG and MEG magnetometers are shown in the Supplementary Materials.).

of this simulation are less reliable.

The additional simulation was based on real average MMN waveforms to the three auditory spectral deviants (pitch, slide, and timbre deviants) from ten single subjects showing clear examples of MMN (see Supplementary Materials). First, the raw curve in the time segment with the MMN in its peak EEG channel was regressed on all EEG channels (as described above in methods Section 2.3). Second, the regressed MMN curve was subtracted to isolate interference and noise waveforms. The peak amplitude of the regressed MMN curve was scaled to a constant of 5 μV. The amplitudes of the interference and noise waveforms were estimated as the standard deviation of the interference and noise waveforms (Haumann et al., 2016). Next, the interference and noise waveform amplitudes were scaled to match SNIRs from 1 to 10 (0.5–5 μV inverse ratios). Finally, the MMN and interference and noise waveforms were multiplied by their channel weights and mixed by summing their waveforms.

11.3. Extraction of MMN responses from SCA, ICA, and PCA decompositions

The simulated data was decomposed into SCA, ICA, and PCA components and the MMN responses were extracted by following the same procedures as in Studies 2-3. The time range t_{comp} for identifying the MMN was based on the grand average MMN shape for the controlled simulation based on the fitted Gaussian components to the grand average MMN. The time range t_{comp} was based on the single subject MMN for the simulation based on the approximated single subject MMN.

11.4. Measuring the accuracy in extracting the MMN responses

The accuracy of the SCA, ICA, PCA methods for extracting the MMN components was evaluated and compared. The error of each method in extracting the MMN response was evaluated by calculating the mean across channels of the root-mean-squared (RMS) error between the extracted and true MMN waveform within the MMN time range t_{comp}. Since it is assumed that SNIR $>$ 1 (see Methods section 2.4 above), only cases where SNIR $>$ 1 were included in the analysis of the results. The median RMS errors for the MMN responses extracted with SCA, ICA, and PCA and the original uncorrected MMN was compared statistically with Friedmann's ANOVA and Wilcoxon signed-rank tests.

Table 5
Results of linear regressions between depressive traits score (MADRS) and amplitudes of MMN responses to each of six types of stimulus deviants. Bonferroni-corrected significance level is $p = .05 / 6 = .008$.

Original signal

Deviant	β	df	t	p	F	p	r^2
Pitch	1.80	73	3.13	.003*	9.81	.003*	.12
Slide	2.21	73	3.89	< .001*	15.11	< .001*	.17
Timbre	1.31	73	2.40	.019	5.77	.019	.07
Intensity	0.38	73	1.16	.248	1.35	.248	.02
Location	1.23	73	1.50	.139	2.24	.139	.03
Rhythm	0.21	73	0.85	.396	0.73	.396	.01

SCA components

Deviant	β	df	t	p	F	p	r^2
Pitch	1.90	73	2.96	.004*	8.79	.004*	.11
Slide	2.58	73	4.13	< < .001 *	17.02	< < .001 *	.19
Timbre	1.96	73	3.15	.002*	9.93	.002*	.12
Intensity	0.34	73	0.89	.378	0.79	.378	.01
Location	1.09	73	1.21	.229	1.47	.229	.02
Rhythm	0.35	73	2.33	.022	5.44	.022	.07

ICA components

Deviant	β	df	t	p	F	p	r^2
Pitch	1.65	73	3.08	.003*	9.50	.003*	.12
Slide	2.28	73	3.64	< .001*	13.24	< .001*	.15
Timbre	1.27	73	2.57	.012	6.60	.012	.08
Intensity	0.21	73	0.81	.419	0.66	.419	.01
Location	0.63	73	0.86	.392	0.74	.392	.01
Rhythm	0.03	73	0.67	.449	0.45	.449	.01

PCA components

Deviant	β	df	t	p	F	p	r^2
Pitch	1.85	73	2.89	.005*	8.36	.005*	.10
Slide	2.58	73	4.04	< .001*	16.31	< .001*	.18
Timbre	1.44	73	2.31	.024	5.33	.024	.07
Intensity	0.28	73	0.82	.415	0.67	.415	.01
Location	1.30	73	1.48	.144	2.19	.144	.03
Rhythm	0.33	73	2.41	.019	5.79	.019	.07

12. Results of study 4

For the simulation with controlled realistic Gaussian signals the RMS error at SNIR > 1 differed significantly dependent on whether the applied method was SCA, ICA, PCA, or the original uncorrected waveforms, $\chi^2(1845) = 2077.13$, $p < < .001$ (Fig. 9 top and Fig. 10). In comparison to the RMS error for the original uncorrected waveforms (median = 1.037) only the SCA method showed a consistent reduction in the RMS error (median = 0.731) ($p < < .001$) (Fig. 9). No significant reduction in RMS error was observed for ICA (median = 1.089) ($p = .474$) or PCA (median = 1.076) ($p = .174$) compared to the original uncorrected waveforms. The RMS error was significantly lower for SCA compared to ICA ($p < < .001$) and PCA ($p < < .001$). Also, there was a tendency of the RMS error to be lower for PCA compared to ICA ($p = .004$).

The patterns in the RMS error heat maps shown in Fig. 10 suggest that the higher RMS errors for the ICA and PCA compared to the SCA method might be related to the constructive and destructive interference patterns between the MMN, alpha, and P3a. Throughout, the effect of P3a amplitude is seen to be less determining for the RMS error than alpha amplitude. Interestingly, this is not the case for ICA where islands of high RMS error are seen instead of the banded appearance of the heat maps in most of the other cases. In a few cases the simulations reveal very noisy RMS landscapes with abrupt changes between neighboring simulation point in the heat map. These likely represent areas where the RMS error is so low that stable estimation would require many more simulation steps. In the PCA heat maps the simulations show RMS error to flatline except for small areas in the region of low P3a and alpha amplitudes. These areas were retained in order to have the same parameter span in all heat maps.

For the simulation with approximated real signals the RMS error at SNIR > 1 also differed significantly dependent on the applied method, $\chi^2(300) = 424.09$, $p < < .001$ (Fig. 9 bottom). Again, the overall lowest RMS error was achieved with SCA in comparison to ICA ($p < < .001$), PCA ($p < < .001$), and the original waveforms ($p < < .001$) (for further details, see the Supplementary Materials). Also, the PCA waveforms showed less RMS error compared to the ICA ($p < < .001$) and original ($p < < .001$) waveforms. Despite less consistent results with ICA, there tended to be an overall reduction of RMS error with ICA in comparison to the original waveforms ($p < < .001$).

13. Discussion

We here proposed that the large-scale activity in neural networks measured with MEG/EEG can be described by spike timing probability density functions. In the first study we show that Gaussian probability density functions consistently and with high-accuracy model neural sources originating from the brain obtained with MEG and EEG measurements, while the Gaussian functions were unable to model artifactual non-encephalic signals. The results of the second study show that the Gaussian probability density functions can be applied to isolate a specific evoked response (ER) of interest, and it is found that the isolated component of interest is represented with higher accuracy with the SCA method than in the original MEG/EEG waveform and in ICA and PCA decompositions. In the third study we show that the SCA method is more reliable compared to ICA and PCA for the analysis of inter-individual differences in ERs, which is relevant to clinical diagnosis. Finally, in the fourth study we observe that the SCA method better than ICA and PCA reduces error caused by interfering neural signals on simulated brain responses at SNIR > 1. The findings from the four studies presented here suggest that the introduced spike density component analysis (SCA) method offers a higher standard of single-subject MEG/EEG analysis than achievable with original data or decompositions with ICA or PCA.

13.1. Modelling MEG/EEG waveforms as Gaussian mixtures

The SCA method uses Gaussian parametric modelling to decompose multichannel MEG/EEG waveforms into Gaussian components. Other MEG/EEG research has utilized Gaussian Mixture Models (GMM), either to estimate soft boundaries for classification or decoding of features based on summary statistics derived from MEG/EEG recordings (Ahmed et al., 2016; Cruz-Garza et al., 2014; Gu et al., 2014; Hasan and Gan, 2010; Yaghouby and Sunderam, 2015; Yuan et al., 2017), for spatial clustering of EEG source locations (Farahani et al., 2017), or for smoothening time-frequency representations of MEG/EEG recordings and neuronal spike rate recordings (Ba et al., 2014). Results similar to the current Gaussian parametric modelling method might be achievable with GMM. Although, we are not aware of studies applying GMM directly on multichannel MEG/EEG waveforms, and GMM appear to have some limitations in relation to the present approach. GMM is appropriate for estimating parametric solutions for a few mixed Gaussian components, but in the present case a relatively high number of mixed Gaussian components were estimated as optimal solutions for modelling MEG/EEG waveforms (median = 66). Also, when applying GMM the number of latent Gaussian components in the data must be predefined (e.g., see Cruz-Garza et al., 2014), though, the Gaussian SCA modelling approach was successfully able to model the MEG/EEG waveforms using an unknown and highly variable number of Gaussian components (range = 4–160). Furthermore, while GMM can model Gaussian shapes in single-or multidimensional spaces, it is here

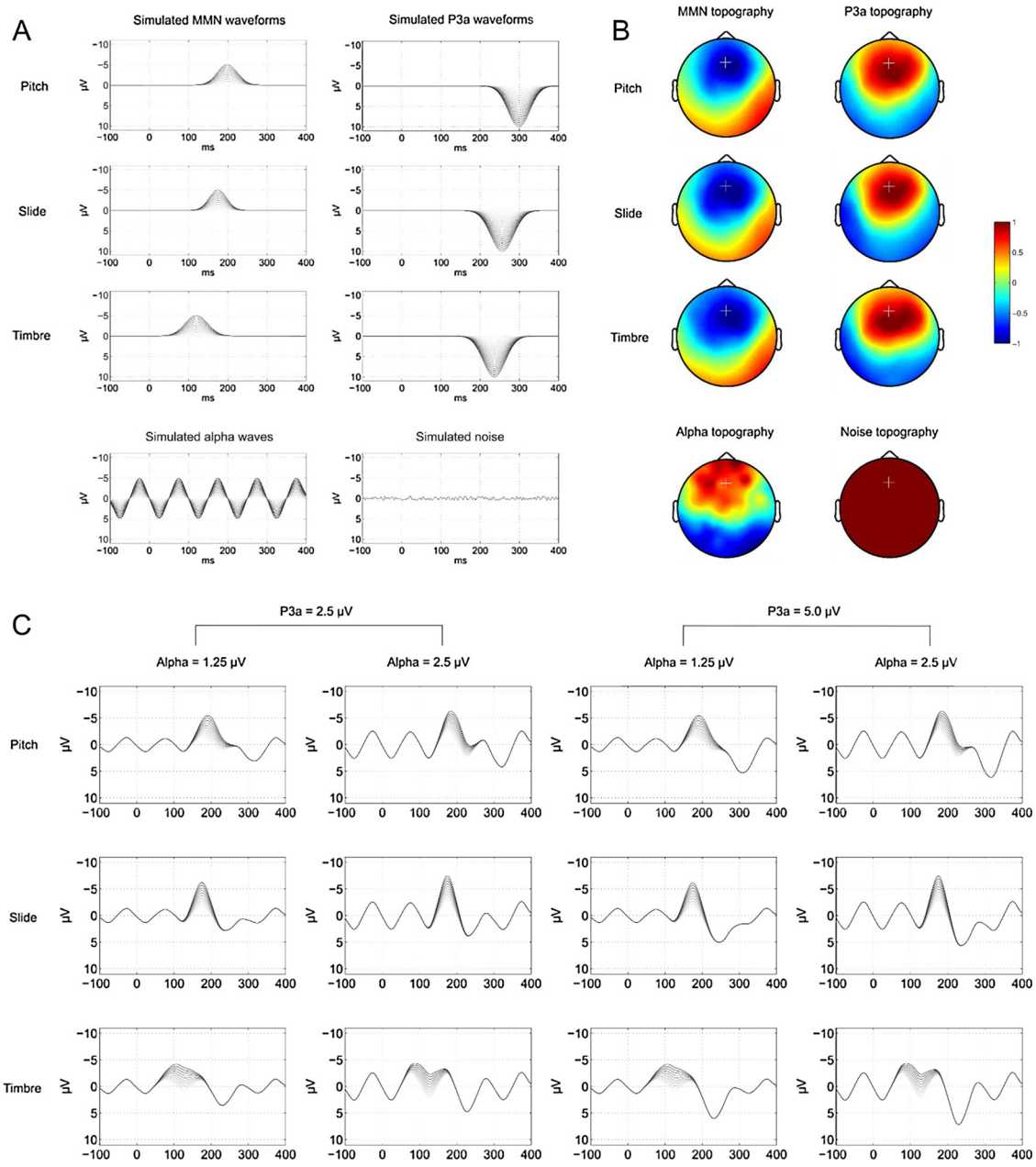

Fig. 8. Simulated signals, interferences, and noise. Waveforms of simulated MMN and P3a responses to spectral pitch, slide, and timbre sound deviants, alpha waves and noise (*A*). The waveforms with darker colors indicate higher amplitudes. The waveforms are weighted by channel weights for the MMN, P3a, alpha, and noise (*B*). The white cross marks the position of the Fz channel for which the waveforms and amplitudes are shown (*B*). Finally, the simulated signals, interferences, and noise are mixed in different amplitude combinations (some examples are shown) (*C*).

necessary to include estimates of spatial weights for projecting each temporal Gaussian component across MEG/EEG channels, and it is not guaranteed that these spatial weights confine to Gaussian shapes.

13.2. Possible role of spike timing in functional specialization

Previous research has suggested that the stochastic spike timing might result from the structure of the dendrite pathways in neural networks (Stein et al., 2005; Teramae and Fukai, 2014). The stochastic spike timing behavior in specific brain regions might introduce certain functional advantages over non-stochastic spike timing for the internal processing of certain types of stimulus features. In particular, the function of learning, and the perceptual and cognitive abilities achieved through learning, is assumed to be implemented in the neural networks through spike-timing-dependent plasticity (STDP) (Barrionuevo and Brown, 1983; Levy and Steward, 1979; Lord et al., 2017; Mcnaughton et al., 1978; Stein et al., 2005). This means that for a general Hebbian type of learning to occur, it is necessary that the spikes between two or more neurons in a neural network, which reflect the neurotransmission process, are overlapping in time. For Hebbian learning based on neurotransmission from lower level areas to be integrated across time, e.g. auditory patterns or visual movements, the STDP in higher level association areas would improve with a stochastic spike timing function for systematically increasing the overlap of the spikes. This explanation is consistent with the observations of larger spike timing distributions widths in cortical association areas (Picton et al., 1974) compared to more narrow spike timing distributions widths observed in the brain stem (Picton et al., 1974), in primary somatosensory cortex (Forss et al., 1994), and in specialized motor and cognitive networks comprising regions of the frontal lobe, basal ganglia and cerebellum (Kelly and

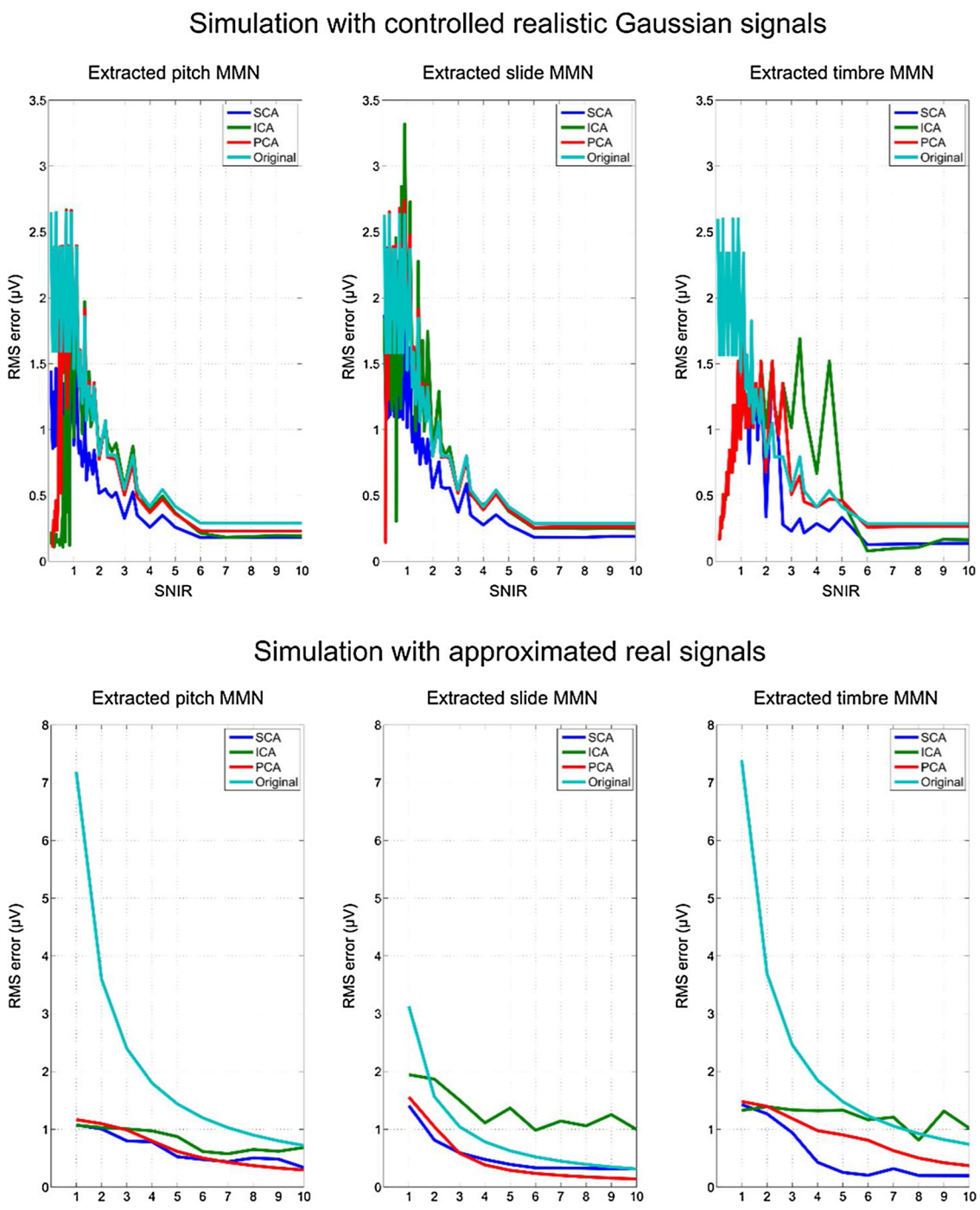

Fig. 9. RMS error of simulated MMN in the original cases and with SCA, ICA, and PCA extraction.

Strick, 2003; Stein et al., 2005), where the last regions are functionally specialized in fast processing and accurate timing (Bostan et al., 2010; Dreher and Grafman, 2002).

13.3. Stochastic neuronal functions in the frequency domain

Until now we have mainly considered MEG/EEG analyses in the time domain. Based on the present theory and findings of low explanatory power of narrowband sinusoids for evoked MEG/EEG signals, it could be considered that the observations of cross-frequency couplings in the frequency domain (Buzsaki et al., 2012; Lakatos et al., 2005) might reflect that high frequency sinusoids are phase-locked to the slower sinusoids, because the lower and higher frequency sinusoids conjointly describe the shape of an underlying non-sinusoidal broadband component. While most MEG/EEG analyses in the frequency domain focus on narrow-band oscillations (Pfurtscheller and da Silva, 1999), in modern signaling theory investigations of signals from sine waves to square pulses have found that the Gaussian function provides an optimal signal shape, which allows a certain amount of timing uncertainty in a communication system (Turletti, 1996). According to the Gaussian minimum-shift keying (GMSK) scheme in signaling theory, the Gaussian function provides an optimal compromise between minimization of the overlap in time and of the occupied frequency bandwidth (related by σ(frequency domain) = 1/σ (time domain)) (Turletti, 1996). Also, a discussion has recently been introduced specifically concerning Gaussian shapes in MEG/EEG power spectra (Haller et al.,

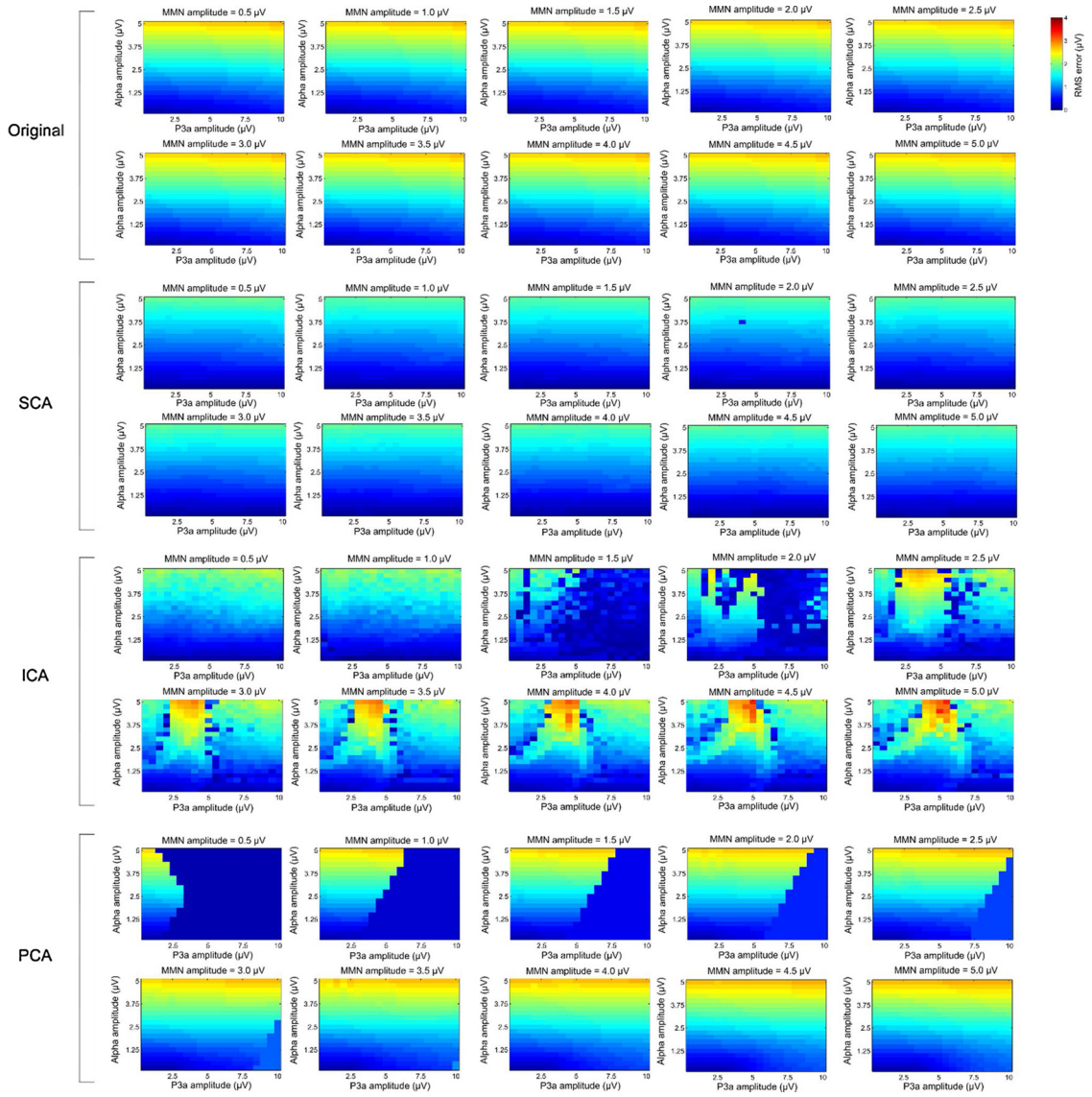

Fig. 10. RMS error heat maps for simulation with controlled realistic Gaussian slide MMN in the original cases and with SCA, ICA, and PCA extraction. (Additional resulting waveforms and the heat maps for the simulated pitch and timbre MMNs are illustrated in the Supplementary Materials.).

2018). The here presented theory of large-scale stochastic neuronal spike trains and the SCA method could provide a theoretical framework and method for estimating the power, peak frequency, and bandwidth and topography of the Gaussian shaped SCA components in the frequency domain.

13.4. Clinical applications of SCA

Auditory brainstem response (ABR) measurement methods are available to indicate stimulus encoding in the brainstem of patients. The short-latency (1 – 10 ms) average evoked ABR can be obtained through the repetition of a brief auditory stimulus (of 40 – 500 ms duration) and application of a high-pass filter (with cut-off frequency at 30 – 100 Hz) to efficiently suppress the relatively slower cortical and external signals (Skoe and Kraus, 2010). However, most cognitive processes occur within the cortex (Duncan et al., 2009), and the problem with overlapping neuronal sources from the cortex is preventing the use of cortical activity, such as the MMN response, in a clinical context with single-subject analysis (Armanfard et al., 2018; Bishop and Hardiman, 2010). We here observe that the SCA analysis provides more accurate isolation and suppression of overlapping cortical sources compared to PCA and ICA. Also, we found that SCA replicates a previously observed effect in a clinical risk population. Hence, SCA allows translation of cortical responses into single-subject clinical diagnostics.

14. Conclusions

We propose that the large-scale stochastic spiking activity observed in MEG/EEG measurements can be accurately described by temporal probability density functions. Findings from our four studies mutually support the assumption, and the findings suggest that single-subject MEG/EEG analysis can be improved with an introduced SCA method in comparison to ICA or PCA. The method and findings presented here are of particular relevance to the investigations on individual differences in brain function and single-subject clinical diagnoses.

Declarations of interest

None.

CRediT authorship contribution statement

Niels Trusbak Haumann: Conceptualization, Methodology, Software, Validation, Formal analysis, Writing - original draft, Visualization. **Brian Hansen:** Writing - review & editing, Supervision. **Minna Huotilainen:** Writing - original draft, Writing - review & editing. **Peter Vuust:** Writing - original draft, Writing - review & editing, Funding acquisition. **Elvira Brattico:** Conceptualization, Resources, Writing - original draft, Writing - review & editing, Supervision, Project administration.

Acknowledgments

This work was supported by the Danish National Research Foundation's Center for Music in the Brain (DNRF117). We thank Marina Kliuchko, Leonardo Bonetti, and Silvia Bruzzone for help in different stages of the project.

Appendix A. Supplementary data

Supplementary material related to this article can be found, in the online version, at doi:https://doi.org/10.1016/j.jneumeth.2020.108743.

References

Ahmed, R., Temko, A., Marnane, W., Lightbody, G., Boylan, G., 2016. Grading hypoxic–ischemic encephalopathy severity in neonatal EEG using GMM supervectors and the support vector machine. Clin. Neurophysiol. 127, 297–309.
Aljadeff, J., Lansdell, B.J., Fairhall, A.L., Kleinfeld, D., 2016. Analysis of neuronal spike trains. Deconstructed. Neuron 91, 221–259.
Armanfard, N., Komeili, M., Reilly, J.P., Connoly, J., 2018. A machine learning framework for automatic and continuous MMN detection with preliminary results for coma outcome prediction. IEEE J. Biomed. Health Inform.
Ba, D.B., Babadi, B., Purdon, P.L., Brown, E.N., 2014. Robust spectrotemporal decomposition by iteratively reweighted least squares. Proc. Natl. Acad. Sci. U. S. A. 111 E5336-E45.
Barbieri, R., Quirk, M.C., Frank, L.M., Wilson, M.A., Brown, E.N., 2001. Construction and analysis of non-Poisson stimulus-response models of neural spiking activity. J. Neurosci. Meth. 105, 25–37.
Barrionuevo, G., Brown, T.H., 1983. Associative long-term potentiation in hippocampal slices. Proc. Natl. Acad. Sci.-Biol. 80, 7347–7351.
Beauducel, A., 2018. Recovering wood and McCarthy's ERP-prototypes by means of ERP-specific procrustes-rotation. J. Neurosci. Methods 295, 20–36.
Bishop, D.V.M., Hardiman, M.J., 2010. Measurement of mismatch negativity in individuals: a study using single-trial analysis. Psychophysiology 47, 697–705.
Bonetti, L., Haumann, N.T., Vuust, P., Kliuchko, M., Brattico, E., 2017. Risk of depression enhances auditory pitch discrimination in the brain as indexed by the mismatch negativity. Clin. Neurophysiol. 128, 1923–1936.
Bonetti, L., Haumann, N.T., Brattico, E., Kliuchko, M., Vuust, P., Sarkamo, T., Naatanen, R., 2018. Auditory sensory memory and working memory skills: association between frontal MMN and performance scores. Brain Res. 1700, 86–98.
Bostan, A.C., Dum, R.P., Strick, P.L., 2010. The basal ganglia communicate with the cerebellum. Proc. Natl. Acad. Sci. U. S. A. 107, 8452–8456.
Bracewell, R.N., Bracewell, R.N., 1986. The Fourier Transform and Its Applications. McGraw-Hill, New York.
Brown, E.N., Kass, R.E., Mitra, P.P., 2004. Multiple neural spike train data analysis: state-of-the-art and future challenges. Nat. Neurosci. 7, 456–461.
Buzsaki, G., Anastassiou, C.A., Koch, C., 2012. The origin of extracellular fields and currents - EEG, ECoG, LFP and spikes. Nat. Rev. Neurosci. 13, 407–420.
Choi, S., Cichocki, A., Park, H.-M., Lee, S.-Y., 2005. Blind source separation and independent component analysis: a review. Neural Inf. Proc. Lett. Rev. 6, 1–57.
Comon, P., 1994. Independent component analysis, a new concept? Signal Proc. 36, 287–314.
Cong, F.Y., Kalyakin, I., Huttunen-Scott, T., Li, H., Lyytinen, H., Ristaniemi, T., 2010. Single-trial based independent component analysis on mismatch negativity in children. Int. J. Neural Syst. 20, 279–292.
Crespo-Garcia, M., Atienza, M., Cantero, J.L., 2008. Muscle artifact removal from human sleep EEG by using independent component analysis. Ann. Biomed. Eng. 36, 467–475.
Cruz-Garza, J.G., Hernandez, Z.R., Nepaul, S., Bradley, K.K., Contreras-Vidal, J.L., 2014. Neural decoding of expressive human movement from scalp electroencephalography (EEG). Front. Hum. Neurosci. 8.
deCharms, R.C., Merzenich, M.M., 1996. Primary cortical representation of sounds by the coordination of action-potential timing. Nature 381, 610–613.
Deco, G., Jirsa, V.K., Robinson, P.A., Breakspear, M., Friston, K.J., 2008. The dynamic brain: from spiking neurons to neural masses and cortical fields. PLoS Comput. Biol. 4.
Delorme, A., Makeig, S., 2004. EEGLAB: an open source toolbox for analysis of single-trial EEG dynamics including independent component analysis. J. Neurosci. Meth. 134, 9–21.
Delorme, A., Plamer, J., Oostenveld, R., Onton, J., Makeig, S., 2007. Comparing results of algorithms implementing blind source separation of EEG data. Swartz Foundation and NIH Grant.
Dien, J., 2010. Evaluating two-step PCA of ERP data with geomin, infomax, oblimin, promax, and varimax rotations. Psychophysiology 47, 170–183.
Dien, J., Beal, D.J., Berg, P., 2005. Optimizing principal components analysis of event-related potentials: matrix type, factor loading weighting, extraction, and rotations. Clin. Neurophysiol. 116, 1808–1825.
Dien, J., Khoe, W., Mangun, G.R., 2007. Evaluation of PCA and ICA of simulated ERPs: promax vs. Infomax rotations. Hum. Brain Mapp. 28, 742–763.
Dorrscheidt, G.H., 1981. The statistical significance of the peristimulus time histogram (Psth). Brain Res. 220, 397–401.
Dreher, J.C., Grafman, J., 2002. The roles of the cerebellum and basal ganglia in timing and error prediction. Eur. J. Neurosci. 16, 1609–1619.
Duncan, C.C., Barry, R.J., Connolly, J.F., Fischer, C., Michie, P.T., Naatanen, R., Polich, J., Reinvang, I., Van Petten, C., 2009. Event-related potentials in clinical research: guidelines for eliciting, recording, and quantifying mismatch negativity, P300, and N400. Clin. Neurophysiol. 120, 1883–1908.
Farahani, E.D., Goossens, T., Wouters, J., van Wieringen, A., 2017. Spatiotemporal reconstruction of auditory steady-state responses to acoustic amplitude modulations: potential sources beyond the auditory pathway. Neuroimage 148, 240–253.
Filali, M., Hutchison, W.D., Palter, V.N., Lozano, A.M., Dostrovsky, J.O., 2004. Stimulation-induced inhibition of neuronal firing in human subthalamic nucleus. Exp. Brain Res. 156, 274–281.
Forss, N., Hari, R., Salmelin, R., Ahonen, A., Hamalainen, M., Kajola, M., Knuutila, J., Simola, J., 1994. Activation of the human posterior parietal cortex by median nerve stimulation. Exp. Brain Res. 99, 309–315.
Friston, K.J., 2005. A theory of cortical responses. Philos. Trans. Biol. Sci. 360, 815–836.
Gaspar, C.M., Rousselet, G.A., Pernet, C.R., 2011. Reliability of ERP and single-trial analyses. Neuroimage 58, 620–629.
Gerstein, G.L., Mandelbrot, B., 1964. Random walk models for the spike activity of a single neuron. Biophys. J. 4, 41–68.
Groppe, D.M., Makeig, S., Kutas, M., Diego, S., 2008. Independent component analysis of event-related potentials. Cogn. Sci. 6, 1–44 Online.
Gu, J.N., Lu, H.T., Lu, B.L., 2014. An integrated Gaussian mixture model to estimate vigilance level based on EEG recordings. Neurocomputing 129, 107–113.
Haller, M., Donoghue, T., Peterson, E., Varma, P., Sebastian, P., Gao, R., Noto, T., Knight, R.T., Shestyuk, A., Voytek, B., 2018. Parameterizing Neural Power Spectra. bioRxiv. 299859.
Hämäläinen, M., Hari, R., Ilmoniemi, R.J., Knuutila, J., Lounasmaa, O.V., 1993. Magnetoencephalography - theory, instrumentation, and applications to noninvasive studies of the working human brain. Rev. Mod. Phys. 65, 413–497.
Hasan, B.A.S., Gan, J.Q., 2010. Unsupervised movement onset detection from EEG recorded during self-paced real hand movement. Med. Biol. Eng. Comput. 48, 245–253.
Haumann, N.T., Parkkonen, L., Kliuchko, M., Vuust, P., Brattico, E., 2016. Comparing the performance of popular MEG/EEG artifact correction methods in an evoked-response study. Comput. Intel. Neurosc.
Jung, T.-P., Humphries, C., Lee, T.-W., Makeig, S., McKeown, M.J., Iragui, V., Sejnowski, T.J., 1998. Removing electroencephalographic artifacts: comparison between ICA and PCA. Neural Networks for Signal Processing VIII, 1998. Proceedings of the 1998 IEEE Signal Processing Society Workshop. IEEE 63–72.
Jung, T.P., Makeig, S., Humphries, C., Lee, T.W., McKeown, M.J., Iragui, V., Sejnowski, T.J., 2000. Removing electroencephalographic artifacts by blind source separation. Psychophysiology 37, 163–178.
Kaiser, H.F., 1958. The varimax criterion for analytic rotation in factor-analysis. Psychometrika 23, 187–200.
Kass, R.E., Ventura, V., Cai, C., 2003. Statistical smoothing of neuronal data. Netw. Comp. Neural. 14, 5–15.
Kayser, J., Tenke, C.E., 2003. Optimizing PCA methodology for ERP component identification and measurement: theoretical rationale and empirical evaluation. Clin. Neurophysiol. 114, 2307–2325.
Kelly, R.M., Strick, P.L., 2003. Cerebellar loops with motor cortex and prefrontal cortex of a nonhuman primate. J. Neurosci. 23, 8432–8444.
Kiebel, S.J., Daunizeau, J., Phillips, C., Friston, K.J., 2008. Variational Bayesian inversion of the equivalent current dipole model in EEG/MEG. Neuroimage 39, 728–741.
Kliuchko, M., Heinonen-Guzejev, M., Vuust, P., Tervaniemi, M., Brattico, E., 2016. A window into the brain mechanisms associated with noise sensitivity. Sci. Rep. UK 6.
Koenig, T., Stein, M., Grieder, M., Kottlow, M., 2014. A tutorial on data-driven methods for statistically assessing ERP topographies. Brain Topogr. 27, 72–83.
Lakatos, P., Shah, A.S., Knuth, K.H., Ulbert, I., Karmos, G., Schroeder, C.E., 2005. An oscillatory hierarchy controlling neuronal excitability and stimulus processing in the auditory cortex. J. Neurophysiol. 94, 1904–1911.
Lee, P.L., Wu, Y.T., Chen, L.F., Chen, Y.S., Cheng, C.M., Yeh, T.C., Ho, L.T., Chang, M.S., Hsieh, J.C., 2003. ICA-based spatiotemporal approach for single-trial analysis of postmovement MEG beta synchronization. Neuroimage 20, 2010–2030.
Lehmann, D., 1989. Microstates of the Brain in EEG and ERP Mapping Studies. Brain Dynamics. Springer, pp. 72–83.
Levy, W.B., Steward, O., 1979. Synapses as associative memory elements in the hippocampal-formation. Brain Res. 175, 233–245.
Litvak, V., Jha, A., Flandin, G., Friston, K., 2013. Convolution models for induced electromagnetic responses. Neuroimage 64, 388–398.
Lord, L.D., Stevner, A.B., Deco, G., Kringelbach, A.L., 2017. Understanding principles of integration and segregation using whole-brain computational connectomics:

implications for neuropsychiatric disorders. Philos. Trans. Math. Phys. Eng. Sci. 375.
Luck, S.J., 2014. An Introduction to the Event-related Potential Technique. MIT Press.
Luck, S.J., Gaspelin, N., 2017. How to get statistically significant effects in any ERP experiment (and why you shouldn't). Psychophysiology 54, 146–157.
Maimon, G., Assad, J.A., 2009. Beyond Poisson: increased spike-time regularity across primate parietal cortex. Neuron 62, 426–440.
Makeig, S., Bell, A.J., Jung, T.P., Sejnowski, T.J., 1996. Independent component analysis of electroencephalographic data. Adv. Neural Inf. 8, 145–151.
Mcnaughton, B.L., Douglas, R.M., Goddard, G.V., 1978. Synaptic enhancement in Fascia Dentata - cooperativity among coactive afferents. Brain Res. 157, 277–293.
Mukamel, R., Ekstrom, A.D., Kaplan, J., Iacoboni, M., Fried, I., 2010. Single-neuron responses in humans during execution and observation of actions. Curr. Biol. 20, 750–756.
Näätänen, R., Kujala, T., Light, G., 2019. Mismatch Negativity: A Window to the Brain. Oxford University Press.
Nikulin, V.V., Nolte, G., Curio, G., 2011. A novel method for reliable and fast extraction of neuronal EEG/MEG oscillations on the basis of spatio-spectral decomposition. Neuroimage 55, 1528–1535.
Oostenveld, R., Fries, P., Maris, E., Schoffelen, J.M., 2011. FieldTrip: open source software for advanced analysis of MEG, EEG, and invasive electrophysiological data. Comput Intel Neurosc.
Pascualmarqui, R.D., Michel, C.M., Lehmann, D., 1995. Segmentation of brain electrical-activity into microstates - model estimation and validation. IEEE Trans. Inf. Technol. Biomed. 42, 658–665.
Pfurtscheller, G., da Silva, F.H.L., 1999. Event-related EEG/MEG synchronization and desynchronization: basic principles. Clin. Neurophysiol. 110, 1842–1857.
Picton, T.W., Hillyard, S.A., Krausz, H.I., Galambos, R., 1974. Human auditory evoked-potentials. 1. Evaluation of components. Electroen. Clin. Neuro. 36, 179–190.
Puce, A., Hämäläinen, M.S., 2017. A review of issues related to data acquisition and analysis in EEG/MEG studies. Brain Sci. 7.
Reynolds, G.D., Richards, J.E., 2009. Cortical source localization of infant cognition. Dev. Neuropsychol. 34, 312–329.
Richards, J.E., 2004. Recovering dipole sources from scalp-recorded event-related-potentials using component analysis: principal component analysis and independent component analysis. Int. J. Psychophysiol. 54, 201–220.
Rodieck, R.W., 1962. Some quantitative methods for the study of spontaneous activity of single neurons. Biophys. J. 2, 351.
Scharf, F., Nestler, S., 2018. Principles behind variance misallocation in temporal exploratory factor analysis for ERP data: insights from an inter-factor covariance decomposition. Int. J. Psychophysiol. 128, 119–136.
Schwartz, D., Badier, J., Bihoue, P., Bouliou, A., 1999. Evaluation of a new MEG-EEG spatio-temporal localization approach using a realistic source model. Brain Topogr. 11, 279–289.
Sharon, D., Hämäläinen, M.S., Tootell, R.B., Halgren, E., Belliveau, J.W., 2007. The advantage of combining MEG and EEG: comparison to fMRI in focally stimulated visual cortex. Neuroimage 36, 1225–1235.
Shimazaki, H., Shinomoto, S., 2007. A method for selecting the bin size of a time histogram. Neural Comput. 19, 1503–1527.
Shin, J., 2002. A unifying theory on the relationship between spike trains, EEG, and ERP based on the noise shaping/predictive neural coding hypothesis. Biosystems 67, 245–257.
Skoe, E., Kraus, N., 2010. Auditory brainstem response to complex sounds: a tutorial. Ear Hear. 31, 302.
Stein, R.B., Gossen, E.R., Jones, K.E., 2005. Neuronal variability: noise or part of the signal? Nat. Rev. Neurosci. 6, 389–397.
Taulu, S., Hari, R., 2009. Removal of magnetoencephalographic artifacts with temporal signal-space separation: demonstration with single-trial auditory-evoked responses. Hum. Brain Mapp. 30, 1524–1534.
Teramae, J., Fukai, T., 2014. Computational implications of lognormally distributed synaptic weights. Proc. IEEE 102, 500–512.
Tong, S., Thakor, N.V., 2009. Quantitative EEG Analysis Methods and Clinical Applications. Artech House.
Tsai, A.C., Liou, M., Jung, T.-P., Onton, J.A., Cheng, P.E., Huang, C.-C., Duann, J.-R., Makeig, S., 2006. Mapping single-trial EEG records on the cortical surface through a spatiotemporal modality. Neuroimage 32, 195–207.
Tseng, T.C., 1949. The normal approximation to the poisson distribution and a proof of a conjecture of Ramanujan. Bull. Am. Math Soc. 55, 396–401.
Turletti, T., 1996. GMSK in a nutshell. Telemedia Networks and Systems Group LCS. MIT-TR.
Vanrumste, B., Van Hoey, G., Van de Walle, R., D'Have, M.R., Lemahieu, I.A., Boon, P.A., 2001. The validation of the finite difference method and reciprocity for solving the inverse problem in EEG dipole source analysis. Brain Topogr. 14, 83–92.
Vigario, R., Sarela, J., Jousmaki, V., Hämäläinen, M., Oja, E., 2000. Independent component approach to the analysis of EEG and MEG recordings. IEEE Trans. Biomed. Eng. 47, 589–593.
Waldert, S., Lemon, R.N., Kraskov, A., 2013. Influence of spiking activity on cortical local field potentials. J. Physiol. London 591, 5291–5303.
Wendel, K., Vaisanen, O., Malmivuo, J., Gencer, N.G., Vanrumste, B., Durka, P., Magjarevic, R., Supek, S., Pascu, M.L., Fontenelle, H., Grave de Peralta Menendez, R., 2009. EEG/MEG source imaging: methods, challenges, and open issues. Comput. Intell. Neurosci., 656092.
Whittingstall, K., Stroink, G., Gates, L., Connolly, J.F., Finley, A., 2003. Effects of dipole position, orientation and noise on the accuracy of EEG source localization. Biomed. Eng. Online 2, 14.
Yaghouby, F., Sunderam, S., 2015. Quasi-supervised scoring of human sleep in polysomnograms using augmented input variables. Comput. Biol. Med. 59, 54–63.
Yuan, S.S., Zhou, W.D., Li, J.H., Wu, Q., 2017. Sparse representation-based EMD and BLDA for automatic seizure detection. Med. Biol. Eng. Comput. 55, 1227–1238.
Zhukov, L., Weinstein, D., Johnson, C., 2000. Independent component analysis for EEG source localization. IEEE Eng. Med. Biol. Mag. 19, 87–96.
Zumer, J.M., Attias, H.T., Sekihara, K., Nagarajan, S.S., 2008. Probabilistic algorithms for MEG/EEG source reconstruction using temporal basis functions learned from data. Neuroimage 41, 924–940.